4
Modeling Nucleation and Growth in Zeolites

C. Richard A. Catlow, David S. Coombes, and Ben Slater
The Royal Institution of Great Britain, London, United Kingdom

Dewi W. Lewis
University College London, London, United Kingdom

J. Carlos G. Pereira
Instituto Superior Técnico, Lisbon, Portugal

I. INTRODUCTION

Modeling techniques have been used for many years in investigations of structures, properties, and reactivities of microporous materials (1). Early work focused on modeling of crystal structures (2), but applications quickly developed in the fields of sorption (see Chapter 9 in this volume) and diffusion (see Chapter 10). In recent years, extensive use has been made of high-level quantum mechanical methods in the study of reaction mechanisms in zeolites (see Chapter 15).

One of the greatest challenges in the current science of microporous solids is to understand at the atomistic level the fundamental processes of nucleation and growth of these materials. Such knowledge, in addition to being of intrinsic value, offers to guide and optimize synthetic strategies. There is a wealth of empirical information on zeolite synthesis, and in the last few years valuable insight has been yielded by the application of light scattering, as well as both small- and wide-angle X-ray scattering and neutron scattering and by time–resolved diffraction studies during hydrothermal synthesis (see, for example, Refs. 3–8). This chapter will focus on our recent applications of modeling methods, which can make a vital and unique contribution to this major field in the science of microporous materials.

II. SCOPE

Our aim is to understand at the atomistic level the process occurring in hydrothermal synthesis, which lead to nucleation and subsequent growth of the crystalline zeolite. To achieve this end we require models for and modeling of the following:

1. The gel chemistry, where in particular we need to develop models of the prenucleation silica and aluminosilica fragments present in the synthesis gels. Knowledge of the mechanisms and energetics of their condensation is also required.

2. The nature of the interactions between silica/aluminosilica species in solution and organic template molecules, in particular the ways in which templates modify the structures and energetics and such structures.
3. The processes of aggregation leading to the formation of zeolite nuclei.
4. The mechanism and rates of the subsequent growth of the zeolite crystal.

The ultimate goal will be to implement the types of modeling described above into a full kinetic model of the whole nucleation and growth process. It will be some time before this aim can be achieved, but considerable progress has been made particularly with regard to 1 and 2 above. This chapter therefore concentrates on recent progress in understanding gel chemistry and templating effects. Very recent advances in understanding aggregation and growth will be discussed toward the end of the chapter. First, however, we need to summarize the main methodologies employed in this field.

III. METHODOLOGIES

To investigate these problems we need to use both ab initio (electronic structure) and molecular mechanics (interatomic potential based) methods. The former are used to model the detailed energies and geometries of the silica fragments, whereas the latter are appropriate for exploring the interaction of the silica species with water and with templating molecules.

In the work reviewed in this chapter, most electronic structure calculations used density functional theory (DFT). A variety of density functionals and basis sets were employed as will be described in greater detail in later sections. Hartree-Fock calculations were, however, performed for a limited number of the calculations reviewed. A variety of software packages are available for such calculations, including DMOL (9) and Gaussian (10).

To model the interaction of the silicate clusters with water, the most effective approach is to combine energy minimization with molecular dynamics techniques. As described in greater detail below, the clusters can be represented using a modified version of the standard, **cvff**, molecular mechanics potential (11); the same parameters may be used in modeling the cluster–water interactions. To model hydration, the clusters are first relaxed to equilibrium and then surrounded by a sheath of water molecules. Full minimization of the cluster–water complex is then undertaken, followed in a number of cases by molecular dynamics and subsequent minimization; the latter procedure will hopefully assist in avoiding local minima. Effective software for undertaking such calculations is the Insight/Discover suite of Accelrys (11,12) as will be described further in a later section.

Additional relevant details will be given in the accounts of the applications that follow.

IV. GEL CHEMISTRY

Our first objective is to gain a more detailed understanding of the structures and energies of key silica clusters and of the energetics and mechanisms of their condensation. Calculations are reported first on clusters in vacuo. Inclusion of the effect of hydration is, however, a crucial feature of our work and is also reported later in this section.

The properties of silica clusters have been studied previously using both experimental and theoretical methods. In the last 15 years, there have been extensive studies of silica species in solution using ^{29}Si nuclear magnetic resonance (NMR), liquid chromatography, vibrational spectroscopy, electron paramagnetic resonances and other experimental techniques (13–19). ^{29}Si NMR spectroscopy proved to be particularly effective in identifying the concentration and gross structural features of such clusters (20–25). However, partly because there are so many different clusters present in solution, it is difficult to study their properties individually using experimental techniques. Recent developments in theoretical methods make it possible to calculate the

structures, energetics, and reactions of silica clusters with improved accuracy, paving the way to a much better understanding of these systems n the future. Previous theoretical work includes semi-empirical (26,27), Hartree-Fock (28–34), and DFT calculations (35–39), plus molecular dynamics simulations (40–42).

We now review the result of recent ab initio calculations on the silica clusters, which we compare, when possible, with available experimental data. Both local (BHL) (43,44) and nonlocal (BLYP) (45,46) calculations, with double numerical (DNP) and triple numerical (TNP) basis sets (47), were used. These results were not corrected by zero point vibrational energy or for basis set superposition error since the accuracy of the calculations is limited by the functional and basis set used, so that this level of complexity is not justified. We discuss all $Si_xO_y(OH)_z$ clusters with a maximum of five silicon atoms, plus some larger clusters including the six-silicon ring and the eight-silicon cube. We consider first the open, noncyclic clusters; then the clusters with a ring; and, finally, the clusters with at least two rings. We present the most relevant conformations for each cluster and analyze the corresponding energetic and structural details. Indeed, our study represents the first detailed conformational analysis of the clusters; we find that hydrogen bonding exerts a critical influence on the conformations calculated. Complex silica clusters are classified according to the NMR notation, $Q^m{}_n$, where n represents the number of silicons which are bonded to m bridging oxygens. In the few cases where this notation proved insufficient, we used e and c for edge and corner, and cis and trans specifications, respectively.

A. Open Clusters

The noncyclic clusters considered in this section vary from the simple monomer and dimer to linear and branched structures containing five Si atoms.

1. Monomer and Dimer: Intramolecular Effects

Although they are too reactive to be found in the gas phase, the monomer and dimer are the most studied silica clusters due to their simplicity and their role as building blocks in the chemistry of silica. The condensation reaction energy in the gas phase depends considerably on the strength of the hydrogen bonds in the dimer.

In the case of $Si(OH)_4$, two conformations are relevant, with point symmetry D_{2d} and S_4. The S_4 conformation is the global minimum in the gas phase and the D_{2d} is a local minimum. The structure and charge distribution for both conformations is presented in Fig. 1. The calculations employed the BLYP density functional with a high-quality TNP basis set. The energy difference between the two conformations is calculated as 1.8 kcal mol^{-1}. Sauer (31) reported a slightly higher value for this energy difference, 3.2 kcal mol^{-1} at the HF/6-31G** and 3.3 kcal mol^{-1} at the HF/6-31G* levels of theory. At the DF-BLYP/TNP level, the *OSiO* angles match exactly the reference HF values (31). While the *SiOH* angle is 2.3° smaller and

Fig. 1 D_{2d} and S_4 $Si(OH)_4$ conformations, optimized at the DF-BLYP/TNP level of approximation.

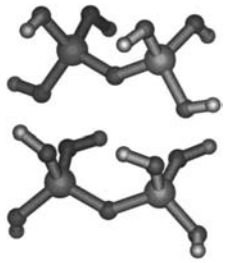

Fig. 2 C_2v and C_2 $Si_2O(OH)_6$ conformations, optimized at the DF-BLYP/TNP level of approximation.

the *SiO* and *OH* bond lengths are only 0.02 and 0.03 Å larger, respectively, than in the HF study. The distance between adjacent hydroxyl groups is too large to allow the formation of hydrogen bonds.

The conformations for the dimer, i.e., the $Si_2O(OH)_6$ cluster, with the lowest energy and the highest symmetry (C_2 and C_{2v} respectively) are presented in Fig. 2, for the DF-BLYP/TNP level of approximation. At this level, the C_2 conformation is +5.7 kcal mol^{-1} more stable than the C_{2v}. This energy difference is substantial and shows the importance of these conformational analyses.

The calculated condensation energies to form the dimer from the monomer:

$$2Si(OH)_4 \rightarrow Si_2O(OH)_6 + H_2O, \quad (1)$$

for the lowest energy conformations are presented in Table 1. At the DF-BHL/DNP level of approximation, the energy is calculated as −9.4 kcal mol^{-1}, but the value decreases to −2.8 kcal mol^{-1} at the DF-BLYP/DNP level and decreases further, to −2.2 kcal mol^{-1}, at the DF-BLYP/TNP level. There are two hydrogen bonds in $Si_2O(OH)_6$ that are not present in the $Si(OH)_4$ reactants, and the simpler BHL/DNP procedure is known to exaggerate the hydrogen bonding energies (39). As in the water dimer (see Table 1), the MP2 prediction (−7.8 kcal mol^{-1}) is smaller than the local DF-BHL/DNP but higher than the best nonlocal DF-BLYP/TNP calculation. Assuming that the difference in energy between local and nonlocal density calculations is due only to the two intramolecular hydrogen bonds occurring in $Si_2O(OH)_6$, the error per hydrogen bond calculated at the DF-BHL/DNP level can be estimated to be about −3.3 kcal mol^{-1}, close to −4.9 kcal mol^{-1}, the corresponding error in the water dimer. The difference between the two values is probably attributable to the *SiOSi* angle requirements that force the hydrogen bonds to be longer than in the water dimer. At the DF-BLYP/TNP level, the *SiOSi* angle is calculated as 132.1°, which seems reasonable, although no experimental results are available for $Si_2O(OH)_6$ in vacuo. We will use the correction of 3.3 kcal mol^{-1} per hydrogen

Table 1 $Si(OH)_4$ Condensation Energy (kcal mol^{-1}) and H_2O Dimerisation Energy (kcal mol^{-1}) after Ab Initio Optimization[a]

Method	Silica condensation	Water dimerization
DF-BHL/DNP	−9.4	−11.3
DF-BLYP/DNP	−2.8	−6.4
DF-BLYP/TNP	−2.2	−4.3
HF/6-31G**	−7.8	−7.1

[a]HF value for the silica condensation from Ref. 31.

bond in later calculations on clusters which, owing to their size, were confined to the DF-BHL/DNP level. However, this is dependent on the corrections being additive and in all the hydrogen bonding terms being equivalent. More rigorous determinations of energies and structures containing hydrogen bonds are now possible using nonlocal density functional calculations.

2. Linear Trimer, Tetramer, and Pentamer: Effects of Ring Formation

We now analyze the linear noncyclic clusters, containing three, four, and five silicon atoms. We find that these clusters can form curved, almost cyclic structures, which can react to form the rings observed experimentally.

a. Linear Trimer

The linear trimer and the trimer ring are the largest silicate clusters studied in this work with nonlocal density functionals. At the DF-BLYP/DNP level of approximation, the lowest energy conformation found for the linear trimer is almost cyclic, with two hydrogen bonds closing the ring. This conformation is 2.2 kcal mol^{-1} more stable than the straight one, where the chain ends are far apart. The structure of both conformations is shown in Fig. 3.

The almost cyclic conformation may, in turn, be transformed into the trimer ring by an intramolecular condensation reaction. The corresponding energy, though positive, is sufficiently small (+13.2 kcal mol^{-1}) to explain how a relatively strained cluster such as the three-silicon ring may be formed.

The hydrogen bonds are overestimated at the DF-BHL/DNP level of approximation, because the O· · ·H distances are too small (~ 1.64 Å) and the OH bond lengths in the acceptor groups are too large (1.02 Å). The condensation energy, at the DF-BHL/DNP level (−18.5 kcal mol^{-1}), is too high when compared with the results for the dimer. Applying the energy difference discussed above, between local and nonlocal DF found for the dimer (3.3 kcal mol^{-1} per overestimated hydrogen bond), the condensation energy is recalculated as −11.9 kcal mol^{-1}. At the DF-BLYP/DNP level, the condensation energy becomes −7.7 kcal mol^{-1}, smaller than even the corrected DF-BHL/DNP value. For this, or for larger clusters with hydrogen bonds, which were studied at the DF-BHL/DNP level, even the corrected values should be considered as an upper limit for the correct results. At the DF-BLYP/DNP level, the O· · ·H and *OH* bond lengths, respectively 1.83 Å and 1.00 Å, are close to the expected values.

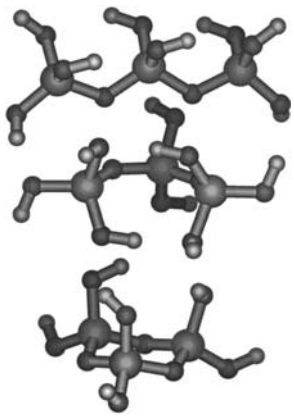

Fig. 3 $Si_3O_2(OH)_8$ conformations forming $Si_3O_3(OH)_6$, optimized at the DF-BLYP/DNP level of approximation.

Recent HF work for this cluster has been reported by Ferrari *et al.* (48) [with SiH_3 instead of $Si(OH)_3$ terminal groups] and Hill and Sauer (32), using symmetry constraints.

b. Linear Tetramer

As in the linear trimer, the lowest energy conformation found for the linear tetramer is almost cyclic, with hydrogen bonds linking the chain ends. At the DF-BHL/DNP level of approximation, this curved conformation is 11.6 kcal mol^{-1} more stable than the straight conformation. The structure and charge distribution for the lowest energy conformations is presented in Fig. 4. The five hydrogen bonds in the curved conformation have an O· · ·H distance that is too short (1.51–1.68 Å) and an *OH* distance that is too large (1.01–1.05 Å), while the six hydrogen bonds in the straight conformation are much weaker.

Although the effect of improving the level of approximation is not clear, it seems reasonable to expect that the curved conformation would still be highly probable. This is in agreement with the experimental evidence, which shows that it is relatively easy to produce four-silicon rings. The easiest way to form a four-silicon ring is probably to close an open four-silicon linear chain, which should be particularly simple starting from this almost cyclic conformation.

The total condensation energy for the curved conformation (−38.2 kcal mol^{-1}) again appears to be too large when compared with the best dimer calculations. Applying the correction factor, previously estimated for each overestimated hydrogen bond, the corrected condensation energy for the most stable conformation is −21.7 kcal mol^{-1}.

Again, we consider that this value might still be too negative.

c. Linear Pentamer

The lowest energy conformation found for the linear pentamer is again almost cyclic, with four hydrogen bonds closing three secondary rings. At the DF-BHL/DNP level, this conformation is 11.4 kcal mol^{-1} more stable than the straight conformation. The structure of the lowest energy conformation is presented in Fig. 5.

The total condensation energy for the curved conformation is substantially negative (−43.6 kcal mol^{-1}). Even after correcting the energy to account for the overestimation of the four hydrogen bonds, the condensation energy is only 1.8 kcal mol^{-1} smaller than that calculated for the uncorrected straight conformation. Therefore, at higher levels of approximation, the almost cyclic conformation should remain highly stable.

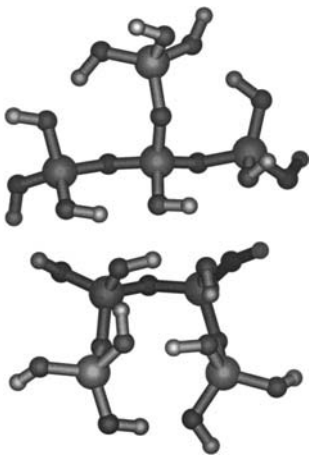

Fig. 4 Noncyclic four-silicon clusters, optimized at the DF-BHL/DNP level of approximation.

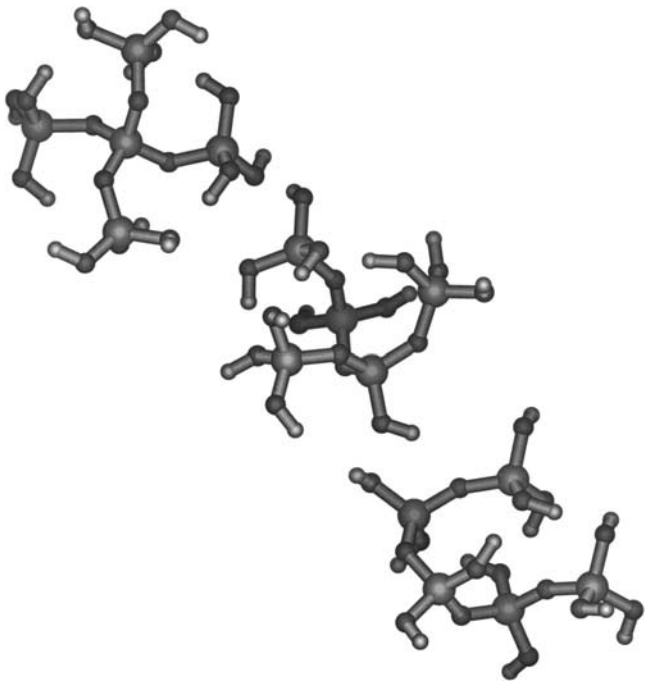

Fig. 5 Noncyclic five-silicon clusters, optimized at the DF-BHL/DNP level of approximation.

This conformation is remarkable because it allows the subsequent formation of several different clusters through a single intramolecular condensation reaction. If each of the four oxygens (marked with an asterisk *) forming hydrogen bonds Si(*)-O-H· · ·O(*)-Si, would react directly with the other silicon (marked with an asterisk *) instead, in a nucleophilic attack four different clusters would be produced: the five-silicon ring, the branched four-silicon ring, the branched three-silicon ring, and the double-branched three-silicon ring.

3. Branched Tetramer and Pentamer Clusters: Branching Effects

In this section, we analyze the branched noncyclic clusters, containing four and five silicon atoms. We find that the branched clusters have higher energies than the linear clusters and should therefore be less stable, in agreement with experiment.

a. Branched Four-Silicon Cluster

The structure of the noncyclic four-silicon clusters is presented in Fig. 4. The proposed conformation for the branched tetramer (above, in the figure) has four hydrogen bonds: two with a reasonable O· · ·H distance (1.80 Å and 2.02 Å) and two with lengths that are too short (1.63–1.64 Å), indicating that the H-bond strengths are overestimated.

Although the condensation energy for the branched tetramer is considerably negative (-30.6 kcal mol^{-1}), it is 7.5 kcal mol^{-1} less favorable than for the linear cluster. This result is in agreement with the experiment evidence, which shows that it is much easier to form the linear than the branched tetramer (22). However, because there are five apparently overestimated hydrogen bonds in the linear tetramer against only two in the branched tetramer, after applying the correction of 3.3 kcal mol^{-1} per hydrogen bond, the energy becomes lower for the branched cluster (-24.0 kcal mol^{-1}) than for the linear cluster (-21.7 kcal mol^{-1}). The

correction may here be exaggerating the relative stability of the branched structure, but the two cluster types probably have similar energies.

b. Branched Five-Silicon Cluster

The structure of the noncyclic five-silicon clusters is again presented in Fig. 5. The most stable conformation found for the branched five-silicon cluster (Fig. 5, center) has four hydrogen bonds which are probably overestimated (O· · ·H = 1.64–1.72 Å), forming three secondary rings. The condensation energy (-40.2 kcal mol^{-1}) is 3.4 kcal mol^{-1} smaller than for the linear chain, decreasing to -27.0 kcal mol^{-1}, when corrected for the hydrogen bonds (compared with -30.4 kcal mol^{-1} for the linear chain). The corrected energy is probably a reasonable estimate in comparison with the values obtained for the previous clusters.

c. Five-Silicon Cross

The best conformation found for this cluster has six hydrogen bonds, forming several secondary rings. The cluster is therefore a good precursor to produce the double-branched three-silicon ring by forming an intramolecular *SiOSi* disiloxane bond.

The condensation energy for the pentamer cross, though relatively large (-32.0 kcal mol^{-1}), is still 8.2 kcal mol^{-1} smaller than for the branched chain (-40.2 kcal mol^{-1}). Taking into account the three overestimated hydrogen bonds, the corrected energy is estimated as -22.1 kcal mol^{-1}, smaller than the corrected energy (-27.0 kcal mol^{-1}) for the branched pentamer. As the condensation energy for the branched pentamer is, in turn, smaller than for the linear chain, it can be concluded that at the LDA level of approximation the cluster stability decreases with the degree of branching, in agreement with the experimental evidence (22). We note that this cluster was also investigated by Lasaga *et al.* (29), using potentials derived from 6-31G* calculations for the monomer and dimer.

The pentamer cross is the only cluster discussed in this chapter where a silicon atom is bonded to four unconstrained bridging oxygens (O_b). The central SiO_b bonds are slightly shorter (1.63–1.64 Å) than the terminal SiO_b bonds (1.64–1.68 Å), though the difference is relatively small. This findings agrees with the experimental and theoretical evidence that the *SiO* bond length tends to decrease in more bridged systems. The *SiO* bond length in α-quartz, [1.60 Å (49), for example] is shorter than the predicted value for $Si(OH)_4$ in the gas phase [about 1.62 Å (31)].

B. Clusters Containing a Single Ring

In our discussion of these clusters we consider first the trimer and tetramer rings, which have particularly relevant conformations; next the branched trimer and tetramer rings, with a lateral chain containing one silicon atom; then the trimer rings containing two silicon atoms in lateral chains; and, finally, the larger, five- and six-silicon rings.

1. Trimer and Tetramer Rings: Ring Conformations

In this section we analyze the smallest silica rings, presenting the most relevant conformations. Trimer and tetramer rings in vacuo are strongly stabilized by an intramolecular cyclic hydrogen bond system.

a. Trimer Ring

Figure 6 shows the three most relevant conformations found in this work for the cyclic trimer. At the DFT-BHL/DNP level of approximation, the bottom conformation (in Fig. 6) is 5.3 kcal

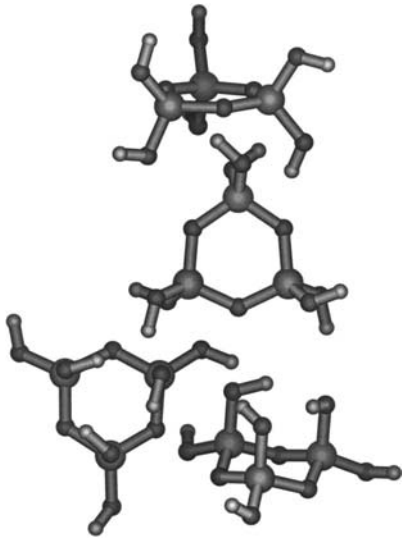

Fig. 6 $Si_3O_3(OH)_6$ conformations, optimized at the DF-BHL/DNP level of approximation.

mol^{-1} more stable than the middle configuration, which in turn is 0.8 kcal mol^{-1} more stable than the upper configuration.

The lowest energy conformation has a *chair* conformation (as in six-carbon rings), where three hydroxyl groups occupy equatorial positions, and the other three are disposed in axial positions, forming a strong system of three hydrogen bonds. At this level of approximation, the total energy of condensation is still exothermic (-1.6 kcal mol^{-1}), despite the strain associated with this ring. At the DF-BLYP/DNP level of approximation, the total condensation energy is already positive but still small (+5.5 kcal mol^{-1}), so it should be present in silica solutions, despite its internal strain, as experiment shows, for low pH (24).

The *SiOSi* angle is much larger in the two planar rings than in the chair conformation ($\sim 116.0°$). The *SiOH* angle assumes two distinct values, one for the equatorial hydroxyl groups ($\sim 114.5°$, as in previous clusters), and another, which is much smaller ($\sim 106.8°$), for the axial hydroxyl groups, that are constrained by the directionality of the hydrogen bonds. However, at the DF-BLYP/DNP level, the O···H distances are relatively long (2.69–3.01 Å).

b. Tetramer Ring

The lowest energy conformation found for the four-silicon ring is a crown conformation [also the most stable conformation in eight-carbon rings (50), which decreases the ring strain and allows the formation of a strong cyclic system of four hydrogen bonds, reducing considerably the energy of the cluster. At the DF-BHL/DNP level of approximation, this conformation is 31.9 kcal mol^{-1} more stable than a planar tetramer, which is more symmetrical but has relatively weak hydrogen bond interactions. The structure of both conformations is presented in Fig. 7. The *SiOSi* angles are much larger (160.4°) in the planar conformation, reflecting the different atomic arrangements of the two rings. The *SiOSi* angle is larger in the four- than in the three-silicon ring.

Although the ring strain should be considerably smaller in this cluster than in the more constrained trimer ring, the total condensation energy for the "crown" conformation (-25.7 kcal mol^{-1}) is probably too negative in comparison with the nonlocal density results obtained for the two- and three-silicon clusters, due essentially to the overestimation by the local density

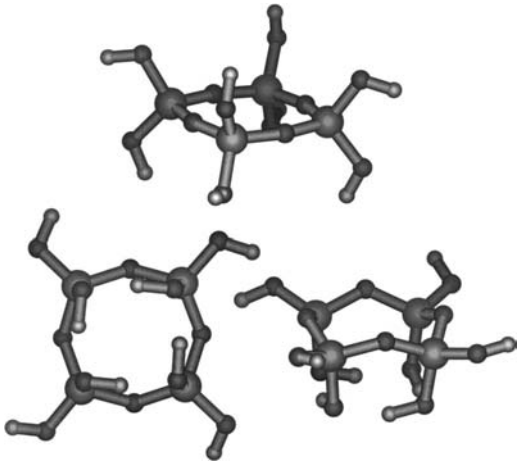

Fig. 7 $Si_4O_4(OH)_8$ conformations, optimized at the DF-BHL/DNP level of approximation.

approximation (LDA) method of the four hydrogen bonds, the lengths of which are too small (~ 1.62 Å). Correcting the energy following the results for the dimer, the condensation energy becomes -12.5 kcal mol^{-1}, which is much more acceptable. Other studies for this ring have been reported by Moravetski *et al.* (34), Hill and Sauer (32), and West *et al.* (26), but only for the planar conformation.

2. Branched Rings: One-Silicon Branched Trimer and Tetramer Rings

We now analyze the simplest branched rings, the trimer and tetramer rings containing a one-silicon lateral chain. Both clusters have a relatively negative condensation reaction energy (from the monomer) and keep the chair and crown conformations found for the nonbranched rings.

a. Branched Trimer Ring

The branched trimer and tetramer rings are presented in Fig. 8. The branched trimer ring (Fig. 8, top) results from the association of a trimer ring (in a chair conformation) with a monomer (in an S_4 conformation), arranged in such a way that a bridging oxygen in the ring forms a

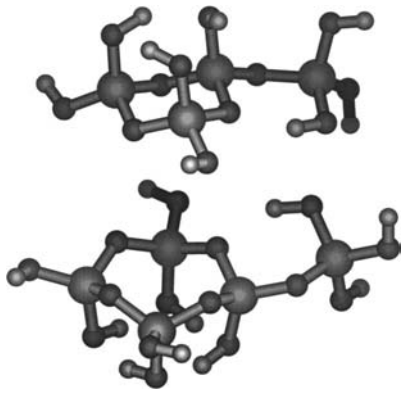

Fig. 8 $Q_2^2Q_1^3Q_1^1$ and $Q_3^2Q_1^3Q_1^1$ clusters, optimized at the DF-BHL/DNP level of approximation.

hydrogen bond with the $Si(OH)_3$ chain. This hydrogen bond introduces a second link between the ring and the chain, in this way increasing considerably the rigidity of the cluster. This hydrogen bond is weaker (1.91 Å) than the three hydrogen bonds in the ring (O· · ·H = 1.85–2.20 Å), which are slightly distorted by the influence of the lateral chain. The length of the *SiO* bond linking the ring and the chain is much shorter (1.61 Å) than the others in the ring or in the chain.

The condensation energy of −6.0 kcal mol^{-1} (i.e., 4.4 kcal mol^{-1} lower than for the three-silicon ring), although relatively small due to the ring strain, is sufficiently negative to result in the significant concentration of this cluster which is usually found in sol-gel solutions (24,25).

b. Branched Tetramer Ring

The branched tetramer ring (see Fig. 8, bottom) is formed by associating a tetramer ring (in a crown conformation) with an S_4 monomer, thus preserving most of the features of these clusters. The lateral chain adds an additional hydrogen bond (O· · ·H = 1.96 Å) to the four hydrogen bonds in the ring (O· · ·H = 1.62–1.65 Å), increasing considerably the rigidity of the cluster, as the lateral chain cannot rotate anymore. The *SiO* bond length is smaller (1.62 Å) than in open chains.

The condensation energy for this cluster of −31.0 kcal mol^{-1} (i.e., 5.3 kcal mol^{-1} lower than for the four-silicon ring) is considerably negative, due to the five hydrogen bonds. When corrected for the four overestimated hydrogen bonds, the energy is estimated as −17.8 kcal mol^{-1}.

3. Branched Rings: Two-Silicon Branched Trimer Rings

We now analyze the four trimer rings containing two silicon atoms in lateral chains. These clusters have similar energies and structural features and should be slightly more stable than the trimer ring.

a. Single-Branched Trimer Ring

The trimer rings with two silicon atoms in lateral chains are presented in Fig. 9. The trimer ring with a single two-silicon chain (Fig. 9, top right) is formed by associating the ring (in the chair conformation) with a dimer (in the C_2 conformation), arranged in order to allow the formation of three hydrogen bonds (two in the lateral chain and one between the chain and the ring), increasing considerably the rigidity of the cluster. The corresponding O· · ·H distances are reasonable (1.94–2.02 Å). Consequently, the calculated condensation energy (−10.95 kcal mol^{-1}) is probably accurate enough not to need any correction.

b. Trans-Branched Trimer Ring

In the *trans*-branched trimer ring (bottom right, Fig. 9), two lateral chains with one silicon each are attached to different silicons on different sides of the ring. There are three hydrogen bonds in this cluster, which are apparently too strong in calculations at the LDA level. However, the differences in length between the various hydroxyl groups are smaller than in previous clusters.

The condensation energy for this cluster (−10.5 kcal mol^{-1}) is only 0.5 kcal mol^{-1} higher than in the previous cluster, but the difference increases after correcting the energy (to −7.2 kcal mol^{-1}) to take into account one possibly overestimated hydrogen bond.

c. Cis-Branched Trimer Ring

The *cis*-branched trimer ring (bottom left, Fig. 9) differs from the previous cluster because the two lateral chains are on the same side of the ring, forming three hydrogen bonds with

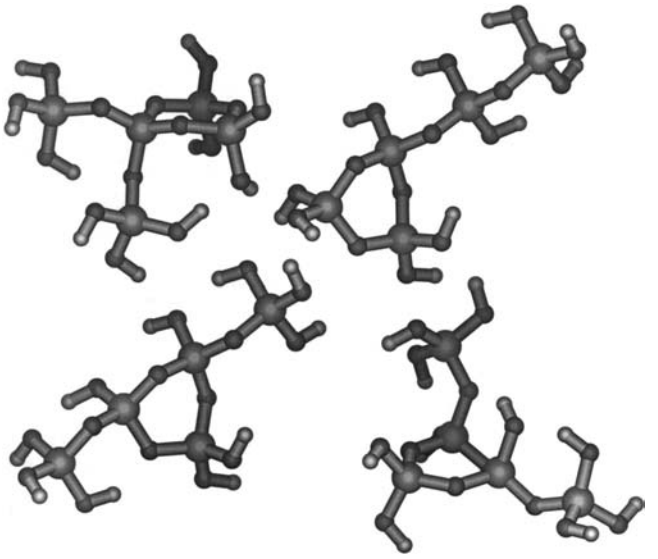

Fig. 9 $Q_2^2Q_1^3Q_1^2Q_1^1$, $Q_2^2Q_2^1Q_1^4$, $Q_2^3Q_2^1Q_1^2$c, and $Q_2^3Q_2^1Q_1^2$t clusters, optimized at the DF-BHL/DNP level of approximation.

reasonable bond lengths (O···H = 1.86–1.90 Å) and a fourth one that is very weak (O···H = 2.74 Å).

The condensation energy for the *cis*-branched cluster (−10.95 kcal mol^{-1}) is almost identical to the energy calculated for the *trans*-branched cluster and matches exactly the energy obtained for the trimer ring with a two-silicon chain, suggesting that, from the energetic point of view, the structural differences between these clusters are irrelevant. The *trans* cluster becomes 3.8 kcal mol^{-1} less stable after correcting its overestimated hydrogen bonds, although there may be some uncertainty in the reliability of the correction in this case.

d. Double-Branched Trimer Ring

In the double-branched trimer ring (top left, Fig. 9), two lateral chains are attached to the same silicon atom in the ring, forming two hydrogen bonds (O···H = 1.66 Å and 1.96 Å), the first one probably overestimated. The condensation energy (−11.3 kcal mol^{-1}) is calculated as roughly equal to or slightly more negative than in the three previous clusters, which is surprising because only two hydrogen bonds exist in this conformation, as opposed to three in the previous clusters.

For all these clusters, the SiO_b bond linking the chain with the ring is strong with bond lengths of 1.61–1.64 Å. In compensation, the next SiO_b bond in the chain is much weaker with bond lengths of 1.66–1.67 Å. These bonds are even longer than in the ring, a trend already noted for the one-silicon branched trimer ring. We also note that the range of variation of the *SiOSi* bond angle is relatively different in the four clusters.

4. Larger Rings: Pentamer and Hexamer Rings

We now analyze the larger five- and six-silicon rings. Our results suggest that, in vacuo, the four- and six-silicon rings are more stabilized by strong hydrogen bond systems than the five-silicon cluster, which lacks the required symmetry, although ring strain factors influence the relative stabilities of the clusters.

a. Pentamer Ring

The five- and six-silicon rings are presented in Fig. 10. The five-silicon ring has the *S-shape* conformation usually proposed for 10-carbon rings (50), but this *S* shape is distorted by four hydrogen bonds formed in this cluster. The hydrogen bond distortions in the five-silicon ring explain the large bond length variations in bridging and terminal groups. The total condensation energy for the five-silicon ring (Fig. 10, top) is smaller (-25.2 kcal mol^{-1}) than for the four-silicon ring (-25.7 kcal mol^{-1}) because the symmetry is much lower, and a cyclic hydrogen bond system is no longer present. However, the LDA corrected energy (-18.5 kcal mol^{-1}) is lower than the value obtained for the tetramer ring (-12.5 kcal mol^{-1}). The larger five-silicon ring allows a better relaxation of the ring strain, though stronger hydrogen bonds may be formed in the four-silicon ring, where the hydroxyl groups are closer to each other.

b. Hexamer Ring

The six-silicon ring (Fig. 10, bottom) has an "extended crown" conformation, with six hydroxyl groups forming a cyclic hydrogen bond system that stabilizes the cluster enormously. These hydrogen bonds seem to be seriously overestimated, as the O$\cdots$H bond lengths (1.56–1.60 Å) are too short and the corresponding O-H bond lengths (1.03–1.04 Å) are too long. Consequently, the total condensation energy for the six-silicon ring (-48.7 kcal mol^{-1}) is likely to be overestimated. The corrected value (-28.9 kcal mol^{-1}) seems to be much more reasonable. In the six-silicon ring, the *SiOSi* angles (127.1–130.0°) are relatively similar to those in the four-silicon ring. The three-, four-, five-, and six-silicon rings discussed here have also been studied by Hill and Sauer (32), using HF with double zeta plus polarization (DZP) and triple zeta plus polarization (TZP) basis sets, but only for the planar conformations, using symmetry constraints. The corresponding condensation energies are more negative than the DF values presented here.

C. Multiple-Ring Clusters

Our analysis of the clusters containing several rings considers first the trimer-trimer double rings, bonded by an edge; second, the trimer-trimer double ring, bonded by a corner, together with the

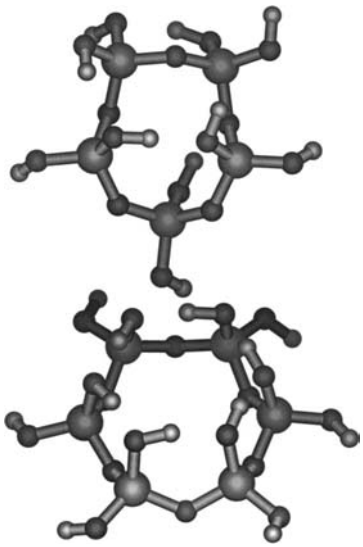

Fig. 10 Large rings, optimized at the DF-BHL/DNP level of approximation.

two tetramer-trimer double rings; and third, the multiple rings: the octamer, the double hexamer, and the sodalite cages.

1. Double Rings: Trimer-Trimer Rings

The double rings, with two intramolecular condensations, are the most strained clusters studied in this work. In this section we analyze the double trimer rings sharing a common edge. In experimental work these clusters are usually not observed.

a. Trimer-Trimer Ring

The structures for the clusters with two trimer rings bonded by an edge are presented in Fig. 11. The four-silicon double ring (Fig. 11, top), which is never found in sol-gel solutions (23–25), is the least stable cluster discussed in this work. This is due to the substantial ring strain of the two rings (both with chair conformations), increased by the additional constraint of sharing a common *SiOSi* edge. Furthermore, only a single hydrogen bond can be formed, at a reasonable distance (2.0 Å), as the two rings force the remaining hydroxyl groups to be too far apart to interact with each other. The condensation energy for this cluster is consequently positive and relatively high (+6.4 kcal mol^{-1}), making its formation very improbable, in agreement with experimental evidence.

The *SiO* bond length changes considerably in the constrained rings but is quite short in terminal groups (only 1.62–1.63 Å). Due to the symmetry of the trimer-trimer framework, the *SiOSi* angles are all relatively similar, for the three clusters ($\sim$122–127°), except the *SiOSi* angle in the edge common to both rings, which is much smaller, but again almost constant ($\sim$113°).

b. Central Branched Trimer-Trimer Ring

The central branched double trimer ring (Fig. 11, bottom left) results from the association of the four-silicon double ring with a monomer in such a way that one silicon is bonded to four bridging oxygens. Both rings have chair conformations, which are very similar to the four-silicon double ring but more planar than in the three-silicon ring.

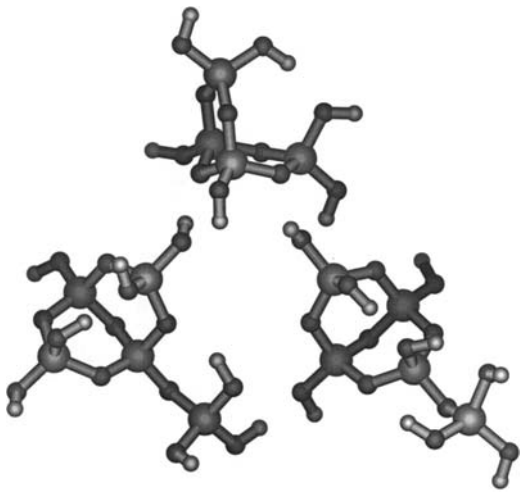

Fig. 11 $Q_2^3Q_2^2$, $Q_2^3Q_1^3Q_1^2Q_1^1$, and $Q_2^2Q_1^4Q_1^3Q_1^1$ clusters, optimized at the DF-BHL/DNP level of approximation.

There are two hydrogen bonds in this cluster, one of which is apparently overestimated. The small condensation energy for this cluster (-0.2 kcal mol^{-1}) is again due to the ring strain and in fact will be more positive due to the overestimated hydrogen bond. The corrected condensation energy of +3.1 kcal mol^{-1} is reasonable, though perhaps slightly too high when compared with the value obtained for the four-silicon double ring (+6.4 kcal mol^{-1}), without the lateral chain and a single hydrogen bond. The *SiO* distances in the rings are relatively large (1.64–1.68 Å), due to the ring strain, but the first *SiO* bond in the lateral chain is very strong: *SiO* = 1.61 Å. This bonding effect is confirmed by the observations made previously for all the trimer branched rings.

c. Outside Branched Trimer-Trimer Ring

The outside branched double trimer ring (Fig. 11, bottom right) differs from the previous cluster in that the monomer is attached to a silicon atom belonging to a single ring, forming a system with two hydrogen bonds, one of which is apparently too short (O· · ·H = 1.75 Å).

The condensation energy (-2.1 kcal mol^{-1}) is slightly lower than for the previous clusters, which is as expected because in the third cluster all silicon atoms are at most attached to three bridging oxygens, whereas in the second cluster a silicon atom was bonded to four bridging oxygens, thereby increasing the cluster strain. The corrected condensation energy (+1.2 kcal mol^{-1}) seems reasonable, given the strain accumulated in the double ring.

2. Double Rings: Corner-Bonded Double Trimer Ring, Trimer-Tetramer Rings

The trimer-trimer double ring with the two rings bonded by a single silicon is discussed here, together with the two tetramer-trimer rings. Although relatively strained, both tetramer-trimer rings have been found in experimental work (24,25), and our calculations also suggest that both clusters should be relatively stable.

a. Corner-Bonded Double Trimer Ring

The corner-bonded double trimer ring and the trimer-tetramer double rings are shown in Fig. 12. In the corner-bonded double trimer ring (Fig. 12, left), two three-silicon rings are

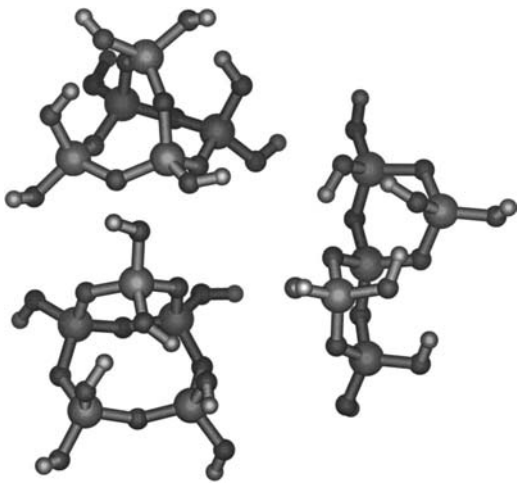

Fig. 12 $Q_4^2Q_1^4$, $Q_2^2Q_2^3Q_1^2e$, and $Q_2^2Q_2^3Q_1^2c$ clusters, conformations at the DF-BHL/DNP level of approximation.

attached to each other by a single silicon atom, instead of a *SiOSi* edge, as in the three clusters before. The conformation proposed here is particularly favorable because it takes advantage of the chair conformation of both rings, which is the least strained cyclic conformation, to allow the formation of four hydrogen bonds that should help considerably to stabilize the cluster.

The condensation energy obtained for this cluster (-1.6 kcal mol^{-1}) is reasonable, though it could be expected that this cluster would be significantly more stable than the two just considered, due to the presence of four hydrogen bonds and because the single corner attachment instead of the shared edge between the two rings should decrease the strain. However, the corrected energy is positive, +1.7 kcal mol^{-1}.

The *SiO* bond lengths change considerably in the double-ring framework (1.62–1.67 Å), essentially due to the different chemical environment seen by the central and outer silicon atoms. The *SiOSi* angle has a surprisingly small range of variation (114.7–122.8°), considering that this is a highly strained cluster, where the environment of the central silicon atom (bonded to four bridging oxygens) is different from that of the other four (bonded to only two bridging oxygens).

b. Edge-Bonded Trimer-Tetramer Ring

In the edge-bonded trimer-tetramer double ring (see Fig. 12, bottom left), a four-silicon ring and a three-silicon ring share a common *SiOSi* chain, where a hydroxyl group in the three-silicon ring forms two hydrogen bonds with *OH* groups in the four-silicon ring, increasing even more the rigidity of the cluster. The three-silicon and four-silicon rings keep the usual chair and crown conformations, but the two hydrogen bonds appear to be too short, i.e., 1.62–1.63 Å.

The bridging SiO_b bond length changes considerably (1.62–1.65 Å), due to the three different silicon environments ($Q^3{}_2$, $Q^2{}_2$, and $Q^2{}_1$) present in the edge-bonded cluster. In the edge-bonded tetramer-trimer ring, the *SiOSi* bond angle is larger (148.2°) in the more relaxed tetramer ring edge opposite to the trimer ring than in the other cyclic bonds (125.9–130.4°).

The condensation energy obtained for this cluster, -13.6 kcal mol^{-1}, is probably too negative, even considering that this cluster is widely found in experimental sol-gel solutions. The corrected condensation energy, -7.0 kcal mol^{-1}, seems to be a more acceptable value for such a strained double ring.

c. Corner-Bonded Trimer-Tetramer Ring

The corner-bonded trimer-tetramer double ring (Fig. 12, top left) differs from the above cluster in that the fragment containing the fifth silicon atom is bonded to two opposite corners of the four-silicon ring, instead of two adjacent ones. Due to this different construction, the crown configuration of the tetramer ring becomes distorted, though two hydrogen bonds are still formed (O$\cdots$H = 1.81–1.82 Å). In this cluster, each bridging oxygen forms a shorter bond (1.62–1.63 Å), and a longer one (1.65–1.66 Å). The $Q^3{}_2$ silicons belonging to both rings have two short and one long SiO_b bonds, while the other $Q^2{}_2$ bridging silicons have two long bonds and the fifth $Q^2{}_1$ silicon two short ones. The O_bSiO_b angles change also considerably (106.6–117.6°). Due to the ring structure, the *SiOSi* angles change considerably, becoming smaller in the four-silicon ring (126.6–135.5°) than in the upper chain (see Fig. 12) formed by the fifth silicon atom (136.3–140.9°).

The corresponding total condensation energy (-8.6 kcal mol^{-1}) is higher than for the edge-bonded ring described above, which is expected, as to form the additional chain over the four-silicon ring should be energetically less favorable than to form a lateral three-silicon ring, as before. When corrected in the usual way, the energy is estimated as -2.0 kcal mol^{-1}, which is probably insufficiently negative, when compared with the double trimer rings, which have almost the same energy and are much less commonly observed in experimental work.

3. Complex Multiple-Rings: Octamer Cage, Double Hexamer Cage, and Sodalite Cage

In this section we analyze the largest silica cluster considered so far: the six-silicon, eight-silicon, 12-silicon, and sodalite cages.

a. Octamer Cage

The most important conformations of the octamer cage are shown in Fig. 13. In one conformation, the rings have a crown arrangement, as in the tetramer ring, whereas in the other they have a nonplanar hexagonal arrangement, where each oxygen is in the plane of one face of the cube and out of the plane of the adjacent face. Each ring in the cage defines a window, which is almost circular in the crown arrangement (of dimensions 3.8 × 3.8 Å) and rectangular in the hexagonal arrangement (of dimensions 4.2 × 3.1 Å).

At the DFT-BHL/DNP level of approximation, the "six-hexagon" conformation is +1.6 kcal mol^{-1} more stable than the "six-crown" conformation. Replacing the hydroxyl groups by hydrogen atoms, the difference in energy between the two conformations decreases to only 0.5 kcal mol^{-1}. The condensation energy to form $Si_8O_{12}(OH)_8$ from the monomer, though positive (+4.1 kcal mol^{-1}), is still smaller than the energy of a single hydrogen bond, which is reasonable for this relatively strained cluster. ^{29}Si NMR experimental evidence shows that this species is relatively stable in solution, at least for high pH values, though it has been found only in small concentrations (20,24,25). The corresponding Hartree-Fock result of Hill and Sauer (32) for the crown conformation, −4.9 kcal mol^{-1} per mole of *SiO* bonds, is surprising for such a constrained cage, which cannot form intramolecular hydrogen bonds.

Experimental *OSiH*, *OSiO*, *SiOSi* bond angles for $Si_8O_{12}H_8$, (~110–112°, 107–109°, and 149–154°) are reviewed by Bornhauser et al. (51). Bond lengths are also given but change considerably in different studies.

b. Prismatic Hexamer, Double Hexamer Cage, and Sodalite Cage

Some of the clusters discussed here, plus the double trimer ring, the double hexamer ring, and the sodalite cage, have been studied recently using Hartree-Fock *ab initio* techniques (32,34).

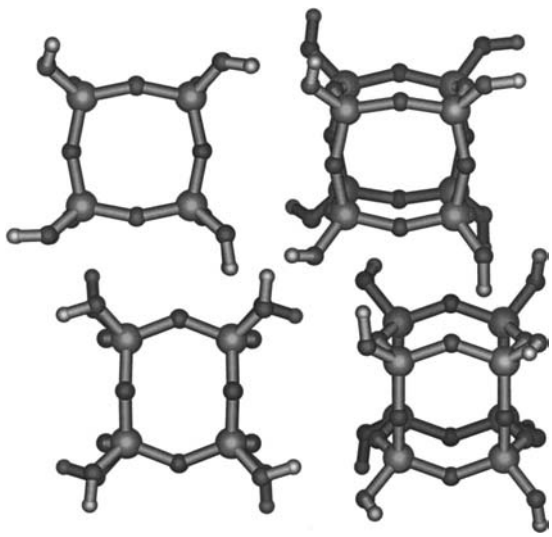

Fig. 13 $Si_8O_{12}(OH)_8$ conformations, optimized at the DF-BHL/DNP level of approximation.

The double trimer ring (prismatic hexamer), $Si_6O_{15}H_6$, can be formed from two trimer rings, positioned one above the other, replacing the three SiOH groups of each ring that interact with the other ring by three SiOSi chains linking the two rings, as if three condensation reactions had occurred. Three lateral tetramer rings are thus formed, producing a considerably strained cluster.

The double hexamer ring, $Si_{12}O_{30}H_{12}$, can be formed from two hexamer rings, positioned one above the other, replacing the six SiOH groups of each ring that interact with the other ring by six SiOSi chains linking the two rings, as if six condensation reactions had occurred. Six lateral tetramer rings are thus formed, producing a relatively strained cluster, though less than the cluster before.

The sodalite cage, $Si_{24}O_{60}H_{24}$, contains eight hexamer rings and six tetramer rings (similar to the Wigner-Seitz cell of a body-centered cubic lattice) and has been studied by ab initio methods (30,32), due to its importance in zeolite studies.

The double tetramer ring (the octamer cage), the double hexamer ring, and the sodalite framework are all so-called secondary building units that can be used to construct complex zeolite structures.

According to these studies (32), the stability increases with increasing ring size as expected from decreasing strain. There is a significant difference between SiO bonds that connect two SiO_4 tetrahedra and SiO bonds connected with a terminal hydroxyl group. The latter are nearly 0.01 Å longer, but the deviations of these bond lengths are the same in both cases. In all molecular models the OH bond has nearly the same length. The lengths of the SiO bonds between the SiO_4 tetrahedra in an Si-O-Si-O-Si chain alternate by nearly 0.02 Å, as found experimentally in quartz (32). The average SiO bond length per SiO tetrahedron remains almost constant, although stretching of one SiO bond leads to shortening of the other SiO bonds of the same tetrahedron.

While the OSiO and SiOH angles fall into the comparatively small ranges of 103–113° and 118–122°, respectively, the SiOSi angle seems to be very flexible. The SiO_4 tetrahedron is obviously a very rigid unit, and the flexibility of the SiOSi angle is responsible for the structural variety of zeolites.

D. Silica Clusters: Summary

Table 2 summarizes the calculated condensation energies discussed above. Overall, when we use corrected energies (i.e., values adjusted for overestimation of the hydrogen bond strength by methodologies based on LDA), the qualitative agreement with experiment is satisfactory in that the clusters with the larger (negative) condensation are observed in silicate solutions. As described in later sections, however, the condensation energies are satisfactorily modified by the effect of hydration, and a full account of the equilibrium distribution of silica clusters in solution will require these effects to be included in detail. Hydration will also modify the hydrogen bonding structure whose importance has been emphasized by the analysis just presented. However, detailed knowledge of the structure and energetics in vacuo is, an essential prerequisite to understanding the properties of the clusters in solution.

E. Aluminosilicate Clusters

Although the majority of both computational and experimental studies have focused on silicate clusters, the properties and stabilities of aluminosilicate clusters are clearly of crucial importance. Indeed, a recent computational study (52) suggested that there is an important influence of the energetics of small aluminosilicate clusters on controlling Si/Al distribution in zeolites. In

Table 2 Condensation Energy (kcal mol^{-1}) for Optimized Silica Clusters[a]

	C_{al}	C_{or}	C_{al}/n	C_{or}/n	C_{al}/s	C_{or}/s	
Q_1^0	-	-	-	-	-	-	1 Si
Q_2^1	−9.4	−2.8	−9.4	−2.8	−4.7	−1.4	2 Si
$Q_2^1Q_1^2$	−18.5	−11.9	−9.3	−6.0	−6.2	−4.0	3 Si
Q_3^2	−1.6	−1.6	−0.5	−0.5	−0.5	−0.5	
$Q_2^2Q_2^1$	−38.2	−21.7	−12.7	−7.2	−9.5	−5.4	4 Si
$Q_3^1Q_1^3$	−30.6	−24.0	−10.2	−8.0	−7.7	−6.0	
$Q_2^2Q_1^3Q_1^1$	−6.0	−6.0	−1.5	−1.5	−1.5	−1.5	
$Q_2^3Q_2^2$	+6.4	+6.4	+1.3	+1.3	+1.6	+1.6	
Q_4^2	−25.7	−12.5	−6.4	−3.1	−6.4	−3.1	
$Q_3^2Q_2^1$	−43.6	−30.4	−10.9	−7.6	−8.7	−6.1	5 Si
$Q_3^1Q_1^3Q_1^2$	−40.2	−27.0	−10.1	−6.8	−8.0	−5.4	
$Q_4^1Q_1^4$	−32.0	−22.1	−8.0	−5.5	−6.4	−4.4	
$Q_2^2Q_1^3Q_1^2Q_1^1$	−11.0	−11.0	−2.2	−2.2	−2.2	−2.2	
$Q_2^2Q_2^1Q_1^4$	−11.3	−11.3	−2.3	−2.2	−2.2	−2.2	
$Q_2^3Q_2^1Q_1^2$cis	−11.0	−11.0	−2.2	−2.2	−2.2	−2.2	
$Q_2^3Q_2^1Q_1^2$trans	−10.5	−7.2	−2.1	−1.4	−2.1	−1.4	
$Q_2^3Q_1^3Q_1^2Q_1^1$	−2.1	+1.2	−0.4	−0.2	−0.4	−0.2	
$Q_2^2Q_1^4Q_1^3Q_1^1$	−0.2	+3.1	−0.0	+0.5	−0.0	+0.6	
$Q_4^2Q_1^4$	−1.6	+1.7	−0.3	+0.3	−0.3	+0.3	
$Q_3^2Q_1^3Q_1^1$	−31.0	−17.8	−6.2	−3.6	−6.2	−3.6	
$Q_2^2Q_2^3Q_1^2$e	−13.6	−7.0	−2.3	−1.2	−2.7	−1.4	
$Q_2^2Q_2^3Q_1^2$c	−8.6	−2.0	−1.4	−0.3	−1.7	−0.4	
Q_5^2	−25.2	−18.5	−5.0	−3.7	−5.0	−3.7	
Q_6^2	−48.7	−28.9	−8.1	−4.8	−8.1	−4.8	6 Si
Q_8^3	+4.1	+4.1	+0.3	+0.3	+0.5	+0.5	8 Si

[a] (C_{al} = calculated; C_{or} = corrected with 3.3 kcal mol^{-1} per H-bond when O· · ·H < 1.85 Å, see text; n = number of condensation reactions to form the cluster; s = number of silicons in the cluster.)

particular, DFT calculations show that the condensation of a silica monomer ($Si(OH)_4$) with an $[Al(OH)_4]^-$ monomer via the reaction:

$$Si(OH)_4 + [Al(OH)_4]^- \rightarrow [SiOAl(OH)_6]^- + H_2O \quad (2)$$

is energetically favorable by 27 kcal mol^{-1}, whereas the formation of *Al-O-Al* bridges by, for example,

$$2[Al(OH)_4]^- \rightarrow [Al_2O(OH)_6]^- + H_2O \quad (3)$$

is endothermic by 41 kcal mol^{-1}. Catlow *et al.* (52) therefore argued that the origin of Lowenstein's rule (53), which forbids *Al-O-Al* bridges in zeolitic and related solids, is probably more associated with the energetics of the reactions involved in forming small clusters, in particular the unfavorable energetics of small clusters and rings containing *Al-O-Al* bridges, rather than with the energetics of the final aluminosilicate crystal structures.

V. HYDRATION EFFECTS

All of the calculations discussed earlier relate to clusters in vacuo. As noted, solvation will, of course, exert a crucial influence on the structures and stabilities of the clusters. However,

calculation of solvation energies is a very difficult problem in theoretical chemistry. A number of different approaches are available ranging from methods in which the solvent is treated as a continuum dielectric to methods in which the solvent is described explicitly (54), but little attention has been paid to the application of these techniques to studying the interaction of silicate fragments with an aqueous environment. The problem of cluster hydration is addressed in this section using a variety of techniques. First, we briefly describe studies of the interaction of small numbers of water molecules with silicate species using ab initio and combined molecular mechanics/ab initio techniques. We then discuss efforts being made to describe the bulk effect of solvation on silicate fragments using both ab initio and (more routinely) molecular mechanics methods.

A. Methods: Techniques and Previous Studies

Considerable attention has been paid to investigating the interaction of silicate species with small numbers of water molecules. The interaction of water molecules with *SiOH* can in general be of two types, with H_2O acting as a proton donor in a hydrogen bond to the oxygen atom of *SiOH* (type I) or H_2O acting as a proton acceptor in a hydrogen bond to the hydrogen of *SiOH* (type II). Calculations using semiempirical methods have indicated that structures of type I are more stable than those of type II (55). However, ab initio calculations (except for those at the STO-3G level) have suggested that the type II structures are more stable than those of type I. Ugliengo *et al.* (56) have carried out calculations on the interaction of a water molecule with silanol H_3SiOH as a model of the isolated hydroxyl of amorphous silica. In addition to the type I and type II structures, they also investigated a bifurcated structure in which both hydrogen atoms of the water molecule interact with the silanol oxygen atom. They confirmed that structure II is most stable, that structure I has a nonplanar stable configuration, and that the bifurcated type II structure is very weakly bound and unstable. Calculations using a 6-31G basis set give interaction energies of -36 kJ mol^{-1} for structure II (57), which is in excellent agreement with the value estimated by Moravetski *et al.* (34) of -30 to -36 kJ mol^{-1} for the average hydration of $Si(OH)_4$ per molecule of H_2O in neutral $H_4SiO_4{\cdot}nH_2O$ complexes.

One method that can be used to model the effect of a solvent with ab initio (or even semiempirical) calculations is the COSMO method developed by Klamt and Schüürmann (58). This method has been introduced into the ab initio DFT code DMol by Andzelm *et al.* (59). The COSMO model is a continuum solvation model where the solute forms a cavity within the solvent of permittivity that is represented by the dielectric continuum. The dielectric medium is polarized by the charge distribution of the solute, and the response of the dielectric medium is described by screening charges on the surface of the cavity.

The free energy of solvation ΔG can be calculated as

$$\Delta G = (E + \Delta G_{nonestatic}) - E^0 \tag{4}$$

where E^0 is the total energy of the molecule in a vacuum, E is the total energy of the molecule in the solvent. $\Delta G_{\text{nonestatic}}$ is the nonelectrostatic contribution from the dispersion and cavity formation effects, which were obtained from fitting the free energies of hydration for linear chain alkanes as functions of surface area (60). For polar, neutral molecules, the calculated hydration energies were in general found to be within 2 kcal mol^{-1} of the experimental value after taking into account the nonelectrostatic contributions, although the agreement was found to be less good for solute ions. Application of the technique to the problem of fragments in solution will be discussed in greater detail below.

Another technique that can be used to estimate solvation energies is the so-called embedded cluster technique (61). Here the bulk solvent is modeled by using a molecular

mechanics (MM) force field and the solute using quantum mechanical (QM) methods. The interaction between the QM and MM regions can be modeled using either mechanical embedding or electrostatic embedding. In mechanical embedding the interactions between the QM and MM regions are modeled using a classical MM force field. In electrostatic embedding the electrostatic potential due to the MM region is included in the QM Hamiltonian. For electrostatic embedding to be successful, the point charges included in the force field have to give a good description of the electrostatic potential, which is unusual since force fields are usually designed to give an accurate description of the total potential and not the individual components of the nonbonded potential. Electrostatic embedding allows polarization effects to be taken into account. Alternatively, polarization due to the environment can be accounted for by using polarizable MM models (62). For QM/MM embedding techniques to be successful the MM force field should be derived using calculations of approximately the same accuracy as those used for the QM region. One such method (63) incorporates solvation polarization using a classical fluctuating charge method, using molecular dynamics to treat the fluctuating charges as dynamic variables. It gave reasonable agreement with high quality ab initio results for a number of dimers involving water. QM/MM techniques have also been used to study the interaction of water with a Brønsted acid site (64). The binding energy of 79.4 kJ mol^{-1} for a water/$Si_2AlO_4H_9$ cluster calculated using a large basis set was found to be in good agreement with a value calculated for the interaction of faujasite with water (65).

B. Calculation of Solvation Energies Using the COSMO Methodology

We have used the ab initio DFT program DMOL together with the COSMO method to estimate the solvation energies for a number of small silicate fragments, shown in Fig. 14. We use a

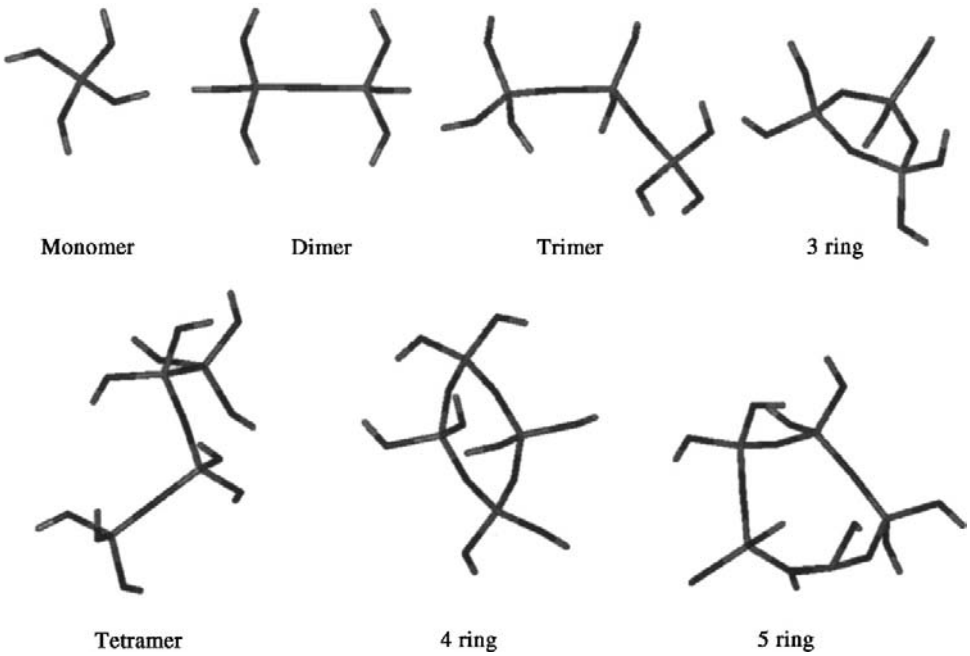

Fig. 14 Silicate fragments used in DMOL/COSMO ab initio and **cvff** molecular mechanics calculations of solvation energy.

Table 3 Calculated Solvation Energies (kcal mol^{-1}) per Silicon Using DMOL/COSMO and **cvff**

Structure	COSMO energy	MM energy
Monomer	−11.3	−11.1
Dimer	−11.1	−8.0
Trimer	−8.4	−6.2
3-ring	−7.8	−7.5
Tetramer	−8.6	−5.1
4-ring	−7.9	−2.6
5-ring	−5.4	−6.9

double numerical atom basis set with polarization (DNP) at the BLYP level of approximation with a medium grid for integration.

The resulting solvation energies are reported in Table 3, which shows that there is a general trend for decreasing solvation energy with increasing silicon content. This is to be expected because the number of OH groups able to form hydrogen bonds with the water molecules decreases. The effect of the solvent on the structure is shown for the five-ring fragment in Fig. 15. The structure in the gas phase is much more open than that in the solvent, and the orientation of the OH groups is different.

We also note that the DFT/COSMO methodology available in DMOL has been used recently to study the mechanism of condensation of silicate monomers to form a dimer species (66). These calculations provided detailed information on the energetics of S_N2-like mechanisms and other activation energies for reactions in the region of 11–16 kcal mol^{-1}. These values accord well with those obtained in recent studies of zeolite nucleation using synchrotron radiation techniques.(67)

C. Molecular Mechanics Methods

By far the most widely used approach to modeling silicate systems and their interactions is to use molecular mechanics force fields. Such methods are widely employed as they are efficient in terms of computer resources and the force fields are parameterized for many different kinds of interactions. Both energy minimization (to obtain energy minima) and molecular dynamics techniques (to sample phase space) are widely employed. Since the energy calculated using a molecular mechanics force field is a sum of bonding (representing the deviations from ideal bond lengths, bond angles, and torsion angles) and nonbonding (representing van der Waals and

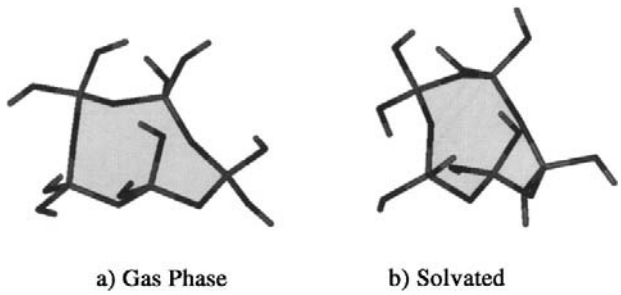

Fig. 15 Comparison of gas phase and DMOL/COSMO optimized five-ring fragment.

electrostatic interactions between nonbonded atoms) terms, it is strictly not correct to compare calculated energies for different molecules, since the "energy zero" calculated using molecular mechanics will be different for different molecules. Comparisons of the energies of different conformations of the same molecule are, however, valid. In this section we describe recent work that has used molecular mechanics methods to explain the solvation of silicate systems in terms of the effect of fragment size and conformation on the calculated solvation energy.

D. Hydration of Small Fragments: Comparison with DFT

When calculating solvation energies, an appropriate model for a solvated system must be constructed. Here there are two choices: either a model where the fragment is surrounded by a "droplet" of water or, alternatively, a calculation employing periodic boundary conditions where the long-range electrostatic interactions in the solvent are taken into account. The solvation energy E_{solv} can then by calculated using the following equation:

$$\Delta E_{solv} = E_{soln} - (E_{solv} + E_{frag}) \tag{5}$$

where E_{soln} is the total energy of the solvent–solute system, E_{solv} is the energy of the solvent, and E_{frag} is the energy of the solute in the gas phase.

We have calculated the solvation energies for the fragments in Fig. 14 using the following method. First, each fragment was solvated out to a distance of 15 Å using the "soak" procedure in the INSIGHTII (12) modeling package, which places the solute in a droplet of water obtained from a molecular dynamics simulation of liquid water and removes the solvent molecules that overlap with atoms of the solute. The total energy of the solute–solvent system was then minimized, whereupon the solute was removed and the minimization repeated to obtain an energy for the pure solvent system. The solvation energy was then calculated according to Eq. (5). In a number of cases the solute–solvent system was subjected to dynamics after which the minimization procedure was repeated. As noted earlier, dynamics was used in an attempt to find the global energy minimum in the solvent–solute system.

The force field used was a variant of the standard **cvff** force field available in the Discover code (11), which was used to perform the energy minimization and molecular dynamics calculations. The modifications introduced improved the accuracy of the Si-O bond lengths (52). The charges used are shown in Table 4.

The calculated hydration energies are shown in Table 3. These results show that the hydration energy per silicon decreases with increasing fragment size—a consequence of the decreasing number of OH groups available for hydrogen bonding with the water molecules for the larger fragments. It is also interesting to note that, in general, similar trends are found in the solvation energies calculated using the molecular mechanics force field and those obtained using the *ab initio* DMOL/COSMO method.

Table 4 Modified Charges in **cvff** Force Field[a]

Atom type	Q (e)
Si	0.46
O	−0.29
H	0.175

[a]For the monomer $Si(OH)_4$ the above charges were used. For the other fragments, the same charges for O and H were used and the charge on Si was varied to ensure electroneutrality.

Calculations to be discussed in greater detail below have also explored solvation effects using an alternative molecular mechanics potential, **cff91_czeo** (32,68). Here the hydration energies obtained are higher by a factor of 2–3 than those found using the modified **cvff** force field. We consider those obtained using **cff91_czeo** to be significantly less reliable than those reported in this section, which are in line with the results of the calculations employing the COSMO technique. However, the **cff91_czeo** force field may yield more accurate structures for the silica fragments.

The sensitivity of the calculated hydration energies to the choice of interatomic potential parameters (particularly to the choice of charges) emphasizes the difficulty of obtaining definitive values for these important quantities. However, we consider that the energies reported in Table 3 represent, reasonable and useful estimates. They will be used in subsequent studies, in combination with the results in Table 2, in order to estimate the equilibrium distribution of clusters in solution.

Next we will discuss the effect of solvation on larger fragments, i.e., those that may form nucleation centers. We will also consider the role of organic templates in stabilizing such prenucleation species. We consider first the geometrical and energetic trends found when fragments are considered as gas phase and solvated species, compared with their "crystalline" state. All the calculations use the **cff91_czeo** (68,32) force field unless otherwise noted.

VI. TEMPLATE-FRAGMENT INTERACTIONS

A. Interactions Between Neutral Silica Fragments, Solvent, and Organic Templates

What effect do water and the organic templates have on the structure and stability of silica clusters, such as those present in a zeolite synthesis gel? We have focused on a specific zeolite, NU-3 (69), isostructural with the mineral levyne (IZA structure code LEV) since there is accurate structural information on the template geometry in the synthesized material for direct comparison. Two templates that are commonly used, 1-aminoadamantane and *N*-methylquinuclidinium (referred to as ADAM and MEQN, respectively), lead to frameworks with a relatively low aluminum content. We have therefore restricted discussions to neutral, silica-only fragments. We have used energy minimization methods to determine the equilibrium geometries and energies of components of the structure of the levyne structure in crystalline, gas phase (*i.e.*, the isolated fragment in a vacuum), solvated, and templated environments. Based on these calculations we will discuss the effect of these various environments on the fragments.

We have constructed 12 different silica fragments that can be extracted from the final crystalline material. These fragments range from the monomeric $Si(OH)_4$ species to entire cages that are present in the structure; the fragments are described in Fig. 16 and Table 5. They were constructed by taking the (energy-minimized) coordinates of the crystalline material and terminating all dangling oxygen bonds with protons.

1. Effect of Crystalline Field

We consider first the stability of the various clusters with respect to the crystalline structure by determining the change in energy and geometry (Table 6) between the fragments constrained to the geometry found in the extended solid (with only the terminating OHs being optimized) and that obtained on full energy minimization in the gas phase (in vaccuo).

We find, in general, that not surprisingly the constrained structures are less stable than those in the gas phase by up to 15 kcal mol^{-1} per Si, although typically about 7 kcal mol^{-1} per Si. Note that we cannot make meaningful comparison between the energies of different

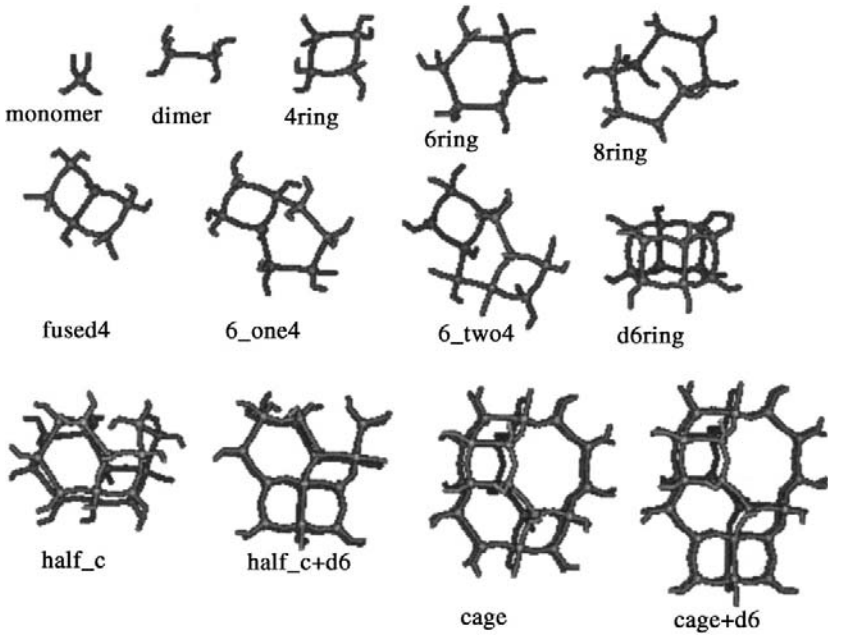

Fig. 16 Silica clusters constructed from the LEV framework structure. Additional descriptions are given in Table 5. Silicon atoms are shown as small spheres.

Table 5 Description of the Fragments Constructed from the LEV Structure Considered in our Calculations

Fragment name	Molecular formula	Molecular mass	Description
Monomer	$Si(OH)_4$	96.1	Monomeric species
Dimer	$Si_2O(OH)_6$	174.2	Bridged dimer
4-ring	$Si_4O_4(OH)_8$	312.4	4-membered ring (MR)
fused4	$Si_6O_7(OH)_{10}$	450.6	Two 4-MRs edge sharing
6-ring	$Si_6O_6(OH)_{12}$	468.6	6-MR
6-one-4	$Si_8O_9(OH)_{14}$	606.8	6-MR edge shared with 4-MR
8-ring	$Si_8O_8(OH)_{16}$	624.8	8-MR
6-two-4	$Si_{10}O_{12}(OH)_{12}$	745.0	6-MR edge shared with two 4-MR at opposite sides
d6ring	$Si_{12}O_{18}(OH)_{12}$	829.2	Double 6-MR
Half-cage	$Si_{18}O_{24}(OH)_{24}$	1297.8	Half of an LEV cage consisting of 4 6-MR and 3 4-MR
Half-cage+d6	$Si_{24}O_{36}(OH)_{24}$	1433.6	As above but with additional 6-MR below base
Cage	$Si_{30}O_{45}(OH)_{30}$	2073.0	Complete LEV cage
Cage+d6	$Si_{36}O_{47}(OH)_{30}$	2433.6	Complete LEV cage with additional 6-MR below base

Table 6 Energies Differences (ΔE) and Surface Areas Changes (ΔSA) Between the Fragments in their Gas Phase (gp), Solvent (solv) and in the Gas Phase in the Presence of the Template 1-Aminoadamantane (ADAMgp) Configurations with Respect to that in their Crystalline Configuration (xtl)[a]

Fragment	ΔE (xtl-gp)	ΔSA (xtl-gp)	ΔE (xtl-solv)	ΔSA (xtl-solv)	ΔE (xtl-ADAMgp)	ΔSA (xtl-ADAMgp)
Monomer	−0.4	1.37	−0.2	2.4	−0.4	0.28
Dimer	−11.9	0.65	−10.0	1.1	−2.8	−0.34
4-ring	−4.8	3.34	−4.4	0.1	−2.7	4.09
Fused-4	−7.8	−1.29	−7.5	−2.4	−7.8	34.88
6-ring	−16.2	0.33	−16.2	−6.9	−2.2	0.58
6-one-4	−13.2	−0.70	−13.0	0.3	−13.1	−0.36
8-ring	−9.5	−0.11	−9.0	−1.6	−9.3	0.40
6-two-4	−11.1	−1.01	−11.0	−10.8	−11.0	−1.45
d6ring	−2.1	−0.37	−1.9	−6.2	−2.0	−0.77
Half-cage	−6.1	−0.12	−5.8	−6.2	−5.8	−0.09
Half-cage+d6	−5.3	−0.58	−5.2	−4.3	−5.1	−0.39
Cage	−7.7	−1.30	−7.5	0.4	−7.6	−1.44
Cage+d6	−7.7	−2.09	−7.6	−2.9	−7.7	−1.88

[a]Energies are in kcal mol^{-1} and areas in $Å^2$.

structures, only between different conformations of the same structure, owing to the definition of the molecular mechanics force field: such a comparison is precluded by the fact that each molecule has a unique energy zero within the molecular mechanics force field. The water-accessible (Connolly) surface area (70) also expands on relaxation, mainly as a consequence of relaxation of the Si-O-Si bond angles from their constrained crystalline configuration. However, there are notable exceptions, such as the eight-membered ring, whose structure changes radically from that present in the solid, with the ring collapsing. Once rigidity is added to the 8-ring, e.g., by the formation of a cage, the structure of this ring is stabilized, suggesting therefore that isolated eight-membered rings are unlikely to feature in the gel and form only as a consequence of condensation between other ring structures. We note that NMR studies have not identified such a structure in silicate solutions. It is also interesting to note the behavior of the 6-ring containing fragments (6-ring, 6_4, and 6_two4): the more open structures containing four-membered rings undergo significant relaxation from their crystalline structure (Fig. 17). In

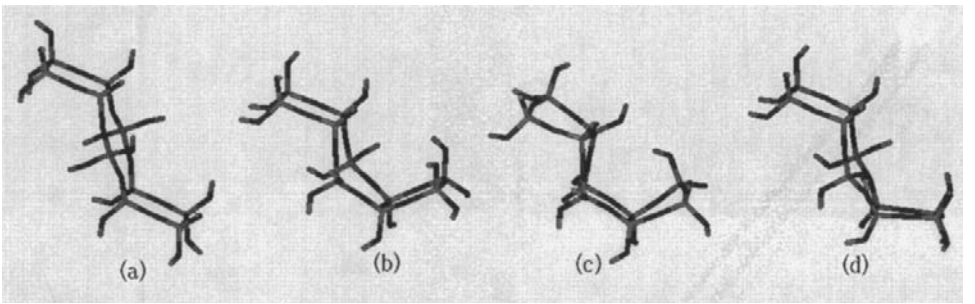

Fig. 17 Geometrical changes in different environments for the 6-two-4 fragment—a single 6-ring with a 4-ring fused at either end (see Fig. 16). (a) Geometry in the crystalline environment, (b) gas phase structure, (c) in solvent, and (d) in solvent and in the presence of the organic template 1-aminoadamantane.

the context of these calculations alone, it is evident that small components of the framework structure are metastable, not only with respect to dense structures but also with respect to the fragments from which they form. Thus, it is necessary to stabilize these fragments in structures in which that they can undertake the geometrical changes required to form the extended lattice. We now consider how solvation affects the conformation and stability of these fragments.

2. Effect of Solvent

Using the same fragments, we have simulated the effect of solvation by placing the fragment in a 15-Å-radius sphere of water and then performing energy minimization. The water-accessible Connolly surface areas and the changes in total surface area on solvation for the fragments considered are given in Table 6. The main feature of these results is the effect of the hydrophobic nature of the silica species resulting in the collapse of the open structure of the fragment. Figure 18 illustrates these changes in terms of the different types of surface area as defined by Connolly (70). In the calculation of the Connolly surface, the probe (water) molecule is in contact with three atoms of the surface in a concave area, two in a saddle area and one in a convex area. Particular emphasis should be made on the contribution of the change in the concave surface area with respect to the total change in surface area clearly showing the hydrophobic nature of the inner surfaces of these clusters. Thus, large open structures, which are not made rigid by the interconnection of rings and cages, collapse inward, reducing their surface area—an effect exemplified by the half-cage fragment. Conversely, the more rigid units, which are self supporting (such as the whole cage fragment), maintain their surface area. The change in surface area appears correlated to the solvation energy of the fragment, as shown in Fig. 19.

The energy gained on solvation generally increases with fragment size, corresponding to the increase in the number of sites, which can form stabilizing (hydrogen bonding) interactions between the solvent and the fragment. Solvation also results in conformational changes in the fragments, resulting in their have a having a higher intramolecular energy than their gas phase structures. The changes in energy from the crystalline configuration of the solvated fragments are lower than those for the gas phase structures (Table 6), i.e., the intramolecular energy of the

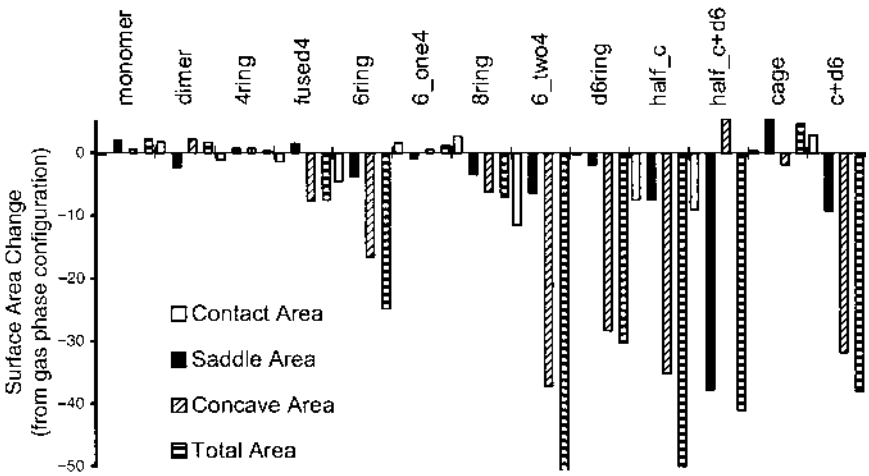

Fig. 18 Changes in water-accessible surface area ($Å^2$) of the LEV fragments on solvation relative to the surface area in the gas phase configuration.

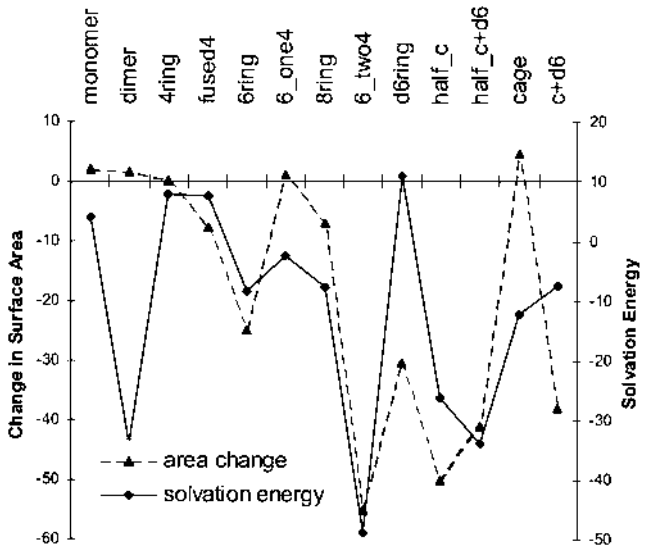

Fig. 19 Correlation between the solvation energy (kcal mol^{-1}) and the change in surface area ($Å^2$) of the LEV fragments.

fragments is higher in the solvent than in the gas phase. Thus, the solvation process goes some way to driving the energy and the geometry of the inorganic species to that in the metastable crystalline structure.

We should note that these calculations do not include any water inside the cage. However, the inside of the cage is usually filled with other species during formation; either the organic template during synthesis or hydrated alkali metal cations (e.g., during the natural formation of levyne). We now consider the effect of organic templates on these fragments.

3. Effect of Template

Both templates, ADAM and MEQN, are encapsulated in the cage of the structure, one molecule per cage, and their geometries have been characterized by X-ray diffraction studies (69). We now consider the interactions of the various fragments with these organic species, first in the gas phase. We have energy minimized the fragment–template assembly, starting from the configuration found in the crystalline structure, and calculated a binding energy defined as:

$$E_{blind}(ft) = E(ft)_g - E(f)_g - E(t)_g \tag{6}$$

where $E(ft)_g$ is the energy of the fragment–template assembly and $E(f)_g$ and $E(t)_g$ are the energies of the fragment and template considered in isolation, respectively.

We present in Table 7 the binding energies together with the change in total surface area from the untemplated fragments of the resulting fragment geometries. From the binding energies we note different trends for the two templates. For the neutral ADAM, we see little increase in the binding energy with fragment size until total encapsulation of the organic occurs. The binding energy of the cationic MEQN, on the other hand, varies considerably with fragment. Here the Coulombic interactions clearly have a greater influence; such effects will be discussed in the next section. However, there is little difference in the effect of the two templates on the *structure* of the fragments. Figure 20 shows the change in the total surface area of the fragments when the crystalline configurations are optimized with and without the

Table 7 Effect of Template on the LEV Fragments[a]

Fragment	Binding energy (kcal mol^{-1})		
	1-Aminoadamantane	Solvated aminoadamantane	1- *N*-Methylquinuclidiunium
Monomer	−51.5	−3.8	−0.4
Dimer	−52.0	−16.9	−11.8
4-ring	−57.7	−2.4	−4.5
Fused-4	−56.9	−59.2	−7.7
6-ring	−55.5	−31.0	−15.9
6-one-4	−56.2	—	−13.1
8-ring	−55.9	−23.3	−9.5
6-two-4	−58.3	—	−11.0
d6ring	−56.0	—	−2.1
Half-cage	−56.9	−17.5	−5.7
Half-cage+d6	−54.8	−19.8	−4.9
Cage	−72.4	−2.8	−7.7
Cage+d6	−73.0	−2.6	−7.7

[a]Shown are the binding energies changes in surface areas and the change in the fragment intramolecular energy (ΔE) from the crystalline configuration.

template being present. In the case of the smaller fragments the presence of the template has little effect, as might be expected. But for the larger fragments, which possess some degree of cage structure, the templates allow the fragments to maintain their open structure, which results in increases in the surface area over the gas phase configuration. However, there does not appear to be a correlation between the binding energy of the templates and this geometrical effect; furthermore, the two templates generally result in similar changes in geometry in the fragments. We can therefore suggest that the short-range van der Waals forces dominate the effect a template has on the *structure*. A similar conclusion is drawn when considering

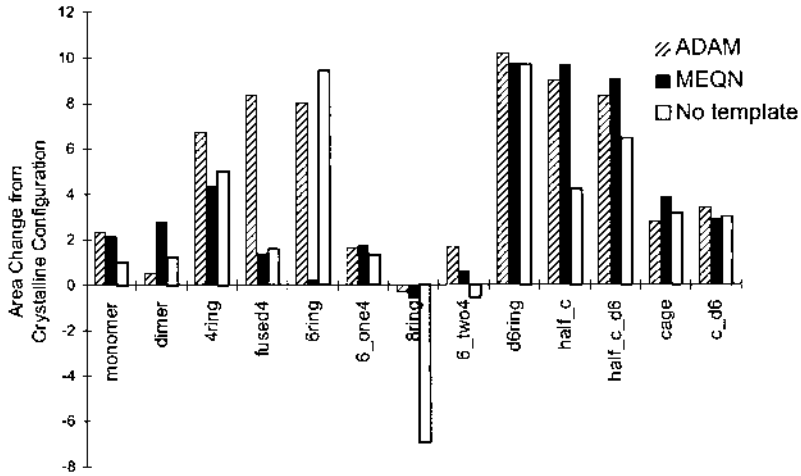

Fig. 20 Change in surface area ($Å^2$) from the crystalline configuration to the gas phase configuration, in the presence and absence of the templates.

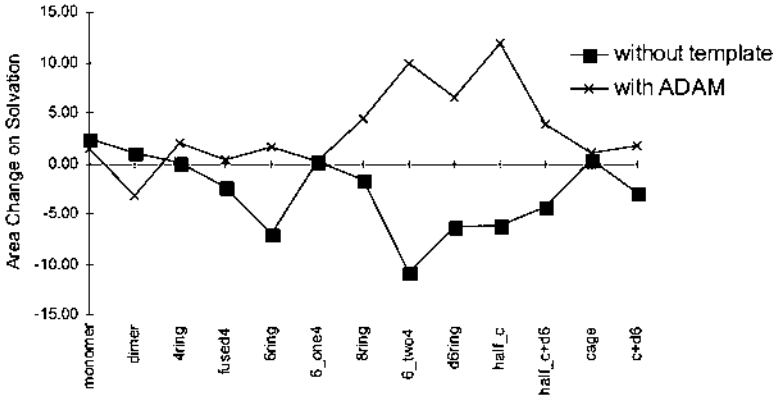

Fig. 21 The effect of the template, 1-aminoadamantane, on the surface area ($Å^2$) of the solvated fragments.

the interaction of templates with the crystalline structure, where here again it is possible to correlate the efficacy of a template at forming a particular structure with the van der Waals interactions between the template and the crystalline framework (71,72). On the other hand, it is clear that the charged nature of the template will have a significant effect on the *binding* of the template to different fragments. This factor will have a direct bearing on the formation of extended structure since the template and fragment must remain "bound" together if further assembly of the framework is to occur. The electrostatic interaction between the template and the fragment will be the dominant contribution to this binding. We shall see later how molecular dynamics simulations can provide additional insights into this phenomenon.

We should also note the effect of the template on the intramolecular energy of the fragment. The change in intramolecular energy of the fragments from the crystalline configuration can be compared to that for the gas phase and in solvent (Table 6). The presence of the template, particularly the charged MEQN, increases the intramolecular energies of the fragments closer to the energy found in the crystalline configuration. Thus, the template provides a further driving force, similar to that seen by solvation (discussed above), by which the inorganic species can be stabilized to allow formation of the metastable crystalline structure.

4. Combined Template–Solvent Effect

We now consider the combined effect of the template and solvent on the fragment and how they interact. It is clear from our discussion to date that the template and solvent have opposing effects on the structures of the fragments considered; the hydrophobic fragments collapse in water, whereas such a collapse is prevented in the presence of the template. Further understanding of these effects is provided by simulation of the effects of adding the template to the solvated fragments (Fig. 21). Again it is clear how the template prevents the decrease in the surface area of the open-structured fragments; the template shields the hydrophobic fragment from the water, preventing collapse of the structure. However, the shielding is not sufficient to compensate for the loss of solvation of the template as illustrated by the reduction in binding energy of the ADAM template and the fragment in solvent given in Table 7. Here we are considering the following process:

$$(\text{Fragment})_{H_2O} + (\text{template})_{H_2O} \rightarrow (\text{fragment} + \text{TPA})_{H_2O} \quad (7)$$

For the unsolvated system we see (Table 7) that for ADAM the binding energy is about 50 kcal mol^{-1} regardless of fragment size. However, upon solvation, the binding energy is reduced, in some cases significantly so. Thus, the removal of solvent from around the template and fragment is not compensated for here by the interactions between the template and the fragment. Thus, these results suggest that neutral templates and neutral silica fragments will not be bound and are, therefore, unlikely to grow further in nucleation centers. Coulombic interactions are therefore seen as crucial to the successful binding and subsequent growth of such fragments. This is discussed further in the next section.

B. Stability of Template–Fragment Complexes in a Hydrated Environment

If synthesis is to proceed via the condensation of monomers and/or small fragments around the template, then it is necessary for such template–fragment complexes to be stable in an aqueous environment. In particular, the complexes must remain bound for a sufficient period of time to permit subsequent reactions to occur. Although the above work has shown that such complexes are often bound, no consideration was taken of the evolution over time of these fragment–template complexes.

We have therefore investigated various aspects of the stability of a range of complexes using both molecular mechanics energy minimization and molecular dynamics techniques. The clustering of monomeric species around tetrapropylammonium, a template used in the synthesis of zeolite ZSM-5, was taken as a typical case. During the synthesis of ZSM-5 the tetrapropylammonium (TPA^+) is encapsulated so that it lies at the intersection of the system of straight and sinusoidal channels in the structure. These calculations were performed using the modified **cvff** force field described earlier. We therefore note that it is difficult to compare these results with those obtained above.

First, we calculated the binding energy between the TPA^+ cation and $Si(OH)_4$ monomers. A neutral TPA species was also created by adjusting the charges on the N, C, and H atoms. In practice the cation will in many circumstances be associated with a charge-compensating ion, particularly when all-silica systems are considered. Energy minimizations were performed on the isolated species. Between one and 16 monomers were then introduced around the TPA cation, energy minimized, and the binding energy obtained. The results for one, eight, and 16 bound monomers are given in Table 8. We note that the complexes are only weakly bound with a binding energy of about 3–5 kcal mol^{-1} per monomer. No significant differences are found in the binding energies and geometries for the TPA and TPA^+.

Next we investigated the binding of water to the TPA cation. As noted in Table 8, the binding of a single water molecule to TPA^+ at about 9 kcal mol^{-1} is considerably greater than

Table 8 Binding Energy of Neutral $Si(OH)_4$ Monomers and Water to TPA^+ and Neutral TPA

Complex	Binding energy (kcal mol^{-1})
$TPA^+/[Si(OH)_4]$	−2.6
$TPA/[Si(OH)_4]$	−2.5
$TPA/8[Si(OH)_4]$	−31.9 (4.0)[a]
$TPA/16[Si(OH)_4]$	−85.1 (5.3)[a]
TPA^+/H_2O	−8.9

[a]Value in parentheses is the binding energy per monomer.

Table 9 Calculated Hydration Energies for the Monomeric Silica Species and the TPA Cation

Species	Hydration energy (kcal mol^{-1})
$[Si(OH)_4]$	−11.1
$[Si(OH)_3O]^-$	−149.5
TPA^+	−60.2

that of the neutral $Si(OH)_4$ monomer. The substantial interaction of water with the cation is further underlined by estimates of the hydration energy using the "soaking" procedure described above. The values reported in Table 9 are far greater than the total binding energy of the 16 monomers to the TPA^+ cation.

The simple but significant conclusion of these calculations is that neutral monomers will be unable to compete with water of hydration surrounding the TPA cation in order to form stable complexes. The conclusion is underwritten by and amplified by a series of MD simulations performed on hydrated complexes, where the simple TPA^+–monomer complex was hydrated in a "droplet" of 10 Å radius of water, after which MD of the hydrated species (including full dynamics of the water molecules) was undertaken for 50 ps. We should stress that these simulations are in the truest sense "computer experiments." The inherently chaotic nature of the complex system simulated results in different detailed trajectories for the different simulations. However, the qualitative conclusions of all these experiments were the same. In every case the complex dissociated, with the monomer being expelled to the edge of the droplet with the hydrated TPA remaining in the center. Similar MD simulations on the cluster comprising TPA^+ with 16 $Si(OH)_4$ monomers hydrated to 15 Å radius showed again that the complexes comprising neutral monomers are unstable; in this case, extensive cluster dissociation had occurred after only 5 ps.

We next explored the stability of complexes comprising TPA^+ and silicate anions. Linear silicate fragments containing between one and three Si atoms and ring clusters containing four

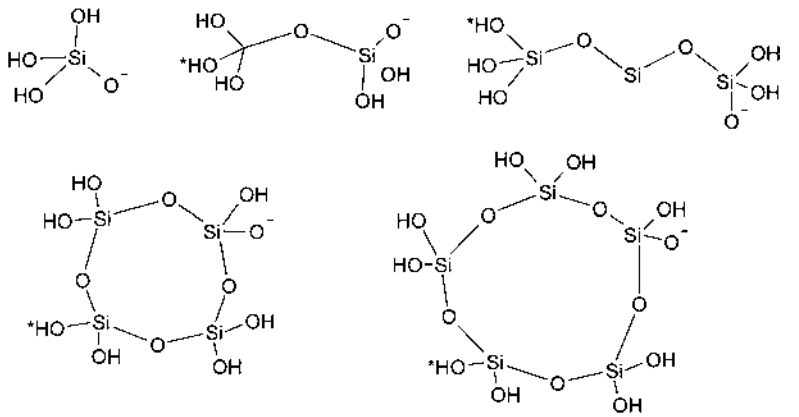

Fig. 22 Charged silica fragments. For the doubly negatively charged species, the second proton removed is indicated by an asterisk (*).

Table 10 Calculated Binding Energies for TPA^+ Complexes with Charged Silica Fragments

Complex	Binding energy (kcal mol^{-1})
$[Si(OH)_3O]^-/TPA^+$	−82.8
$[Si_2(OH)_5O_2]^-/TPA^+$	−81.8
$[Si_3(OH)_7O_3]^-/TPA^+$	−88.5
$[Si_4(OH)_7O_5]^-/TPA^+$	−78.0
$[Si_5(OH)_9O_6]^-/TPA^+$	−86.7
$[Si(OH)_2O_2]^{2-}TPA^+$	−161.4
$[Si_2(OH)_4O_3]^{2-}/TPA^+$	−156.4
$[Si_3(OH)_6O_4]^{2-}/TPA^+$	−153.5
$[Si_4(OH)_6O_6]^{2-}/TPA^+$	−130.8
$[Si_5(OH)_8O_7]^{2-}/TPA^+$	−146.6

and five Si atoms were investigated; their structures are shown in Fig. 22; doubly charged anions were, however, also studied. Calculated binding energies of these species to TPA^+ are reported in Table 10. They are now, as might be expected, substantial. Large increases in hydration energies for the anions as opposed to the neutral species might also be anticipated. The results reported in Table 9 for the singly charged monomer bear out these expectations.

To test the stability of these complexes comprising charged silicate fragments, a series of MD simulations on 10-Å "droplets" were performed as described above. The results are complex but interesting. If we first take the singly charged species, we see that the TPA^+–$(monomer)^-$ complex dissociates over a period of about 30 ps during which the anion is expelled to the edge of the droplet. Over the same period the complex with the dimer anion is more stable but the anion again slowly moves to the edge of the droplet. The trimer complex stays associated over the period, but in longer runs the complex began to dissociate. In 30-ps runs the TPA^+–$(tetramer)^-$ complex also dissociated at the end of the simulations. The complex with the pentamer anion again appears to dissociate slowly over a period of 20 ps. Overall, it appears that complexes with singly charged silicate anions may show some greater stability than neutral fragments; however, in general, they tend to dissociate over periods of about 20–30 ps.

If we now consider complexes with doubly charged anion species, for the monomer we again find dissociation over a period of 30 ps. For the dimer, the complex stays loosely associated but after about 25 ps it has diffused toward the edge of the droplet. However, the complex with the doubly charged anionic trimer stays associated over a period of 30 ps but then begins to dissociate. The complexes comprising the TPA^+ and the double-charged tetramer and pentamer were found to be stable over 30–50 ps, although there is a tendency for the complex to move toward the edge of the droplet. The conclusions we can draw from these experiments are necessarily very tentative. More simulations are needed on larger systems; and it would be desirable to repeat some of the work using periodic boundary conditions. It is clear, however, that stable template–fragment complexes will not form in aqueous solution when the latter are neutral. The stability of the complexes with single-charged anions also seems questionable. It does appear possible, however, that with doubly charged species (which are likely to be present in high pH solutions) complexes with modest-sized fragments may be sufficiently stable to permit further condensation and growth of the silicate fragment. Additional work on the stability of these fragments and their behavior in an aqueous environment is encouraged by these results.

VII. MODELING GROWTH

In previous sections the subject of nucleation has been addressed from a number of perspectives so as to explain the first steps in the formation of gel particles or nanostructures. Once the ordered nanocluster is formed, the crystal enters a growth regime that is largely unexplored via simulation methods but has been extensively studied experimentally. For example, using a combination of high-resolution transmission electron microscopy (HRTEM) and X-ray deffraction it has been shown that for specific cases such as zeolite L (73) and LTA (74), the ordered nanoclusters do not appear to Ostwald ripen (75). Ageing of these particles leads to the growth of faceted crystals, often with extremely well-defined crystal morphology. In the postnucleation regime, the crystal growth is clearly dictated by the relative growth rate of oriented faces. Thus, by using the atomistic techniques that have been widely and successfully applied to study the morphology of metal oxides (76) and minerals, interesting new insights into the growth of microporous crystals are being revealed.

In order to perform meaningful calculations to assess the relative stability of morphologically important faces, it is essential that the surface structure be known or be predicted with certainty. For over a decade, two powerful methods have been used to investigate the exact external surface structure of zeolites: atomic force microscopy (AFM) and HRTEM. Increasingly, the resolution of these techniques is giving important information about the topology of zeolites on the angstrom scale, and analysis of the data reported so far reveals some systematic features. HRTEM data reported by Terasaki (77) and coworkers indicate the presence of well-defined features, which are indicative of nanostructures on faceted surfaces of FAU(111) for example. These observations are further supported by AFM work by Anderson *et al.* (78) and Agger *et al.* (79) on materials such as LTA and FAU, which suggest systematic step heights which can be related structural units or sub-units of the unit cell. However, because of the resolution of the techniques, the exact termination of these structures is not always unequivocal. By using computer simulation methods, one can assess the thermodynamic stability of the proposed surface structures using the thermodynamic stability of surface, or *surface energy.*

In recent work, these techniques have been used to address the surface structure of zeolite beta C (80), a highly topical 12-membered ring zeolite (81). Terasaki reported exceptionally high-quality HRTEM data indicating the presence of two well-defined surface structures on the (110) face. In Fig. 23, the surface topology of zeolite beta C is shown. The first surface structure is that defined by the light gray framework only (termination 1), whereas the second structure is double 4 ring (D4R) terminated and shown in dark gray, and is clearly related to the initial surface structure by the addition of the D4R. A question prompted by this these observations is; why are no intermediate structures observed? For instance, following work described earlier in this chapter, it is conceivable that a multitude of oligomeric species could react with the termination 1 surface structure to produce a variety of different terminations. In particular, why is the single 4 ring (S4R)–terminated surface structure not formed, which could be formed by the condensation of a Q_4 or related open-ring species onto termination 1?

Using classical simulation methods, based on the Born model of solids and the MARVIN code (76), we have explored the possible terminations of the (110) surface described in greater detail elsewhere (80). Screening based on selection of surface cuts with the lowest surface energy gives rise to three possible structures. Two of the cuts are identical to those observed experimentally, but a third cut, which corresponds to an S4R-terminated structure, is found to have identical surface energy (and hence thermodynamic stability) to the two experimentally observed structures. This result implies that observance of all three structures would be expected which is clearly not the case. To understand the origin of this apparent discrepancy between theory and experiment, the direct condensation of S4R and D4R species onto termination 1 was

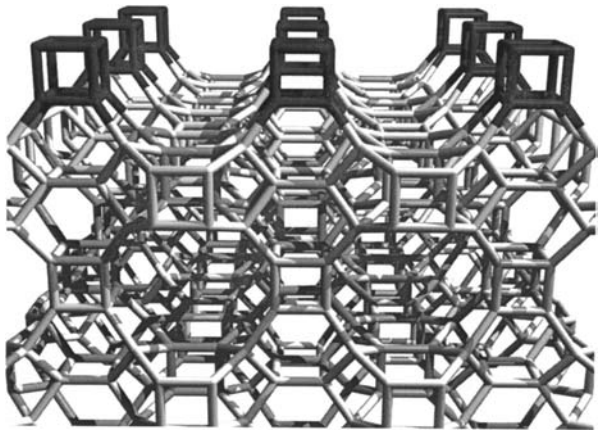

Fig. 23 Surface structure of zeolite beta C (110), where the dark gray layer defines the surface plane. Only the siliceous framework is depicted. The light gray structure has been observed experimentally, as has a second termination generated by condensation of a double 4 membered ring (Q_8) on the growth surface, shown in dark gray.

considered. Using plane wave–based, first-principles methods (82), the direct condensation of an S4R onto the termination 1 surface was found to be thermodynamically unfavorable, though additional condensation of an S4R onto the S4R-terminated structure was found to be energetically viable. In contrast, direct condensation of a D4R onto termination 1 was found to be thermodynamically favorable.

These results suggest that a possible explanation for the absence of an intermediate surface structure with S4R termination is that the reaction does not occur, or that it is kinetically unstable with respect to condensation of an additional S4R to give the D4R terminated structure. Direct condensation of the D4R species is viable under reaction conditions and, in combination with the results of the S4R-mediated reaction pathway study, provides strong evidence that D4R condensation onto the growing surface is an important step in crystal growth of this surface. Furthermore, this observation adds weight to the proposition that zeolite growth may be controlled by the oligomeric species present in the reaction mixture.

Although these findings relate to crystal growth on highly crystalline faces, it will be interesting to investigate whether growth on higher index, more reactive faces shows similar behavior and thus whether insight into amorphous gel to crystallite transformations can be obtained by investigation of growth on crystalline surfaces. In addition, these atomistic computational techniques are being used to investigate how varying the stoichiometry of zeolites leads to substantial changes in observed crystal morphology and how one might effect control of the crystal habit by use of inhibitors or promoters. More generally, the utility of computer simulation methods to understand processes in crystal growth is underlined and illustrates how atomic scale simulation is providing elementary insight into zeolite chemistry in an increasingly predictive manner.

VIII. CONCLUSIONS

We are still some way from having a detailed understanding of the mechanisms of nucleation and growth of zeolites during their hydrothermal synthesis. What we hope to have shown in this chapter is that modeling methods have already made a significant contribution to an understanding of silica cluster structures in synthesis gels and the ways in which they interact

with water and templates. The reader is referred to Refs. 83 and 84 for additional details about the work described here.

Progress is now underway in the simulation of the key processes involved in the growth of zeolites. Improving the understanding of the latter is one of the challenges of the field. Developing good models for structures and energetics of critical nuclei is also a key requirement. As commented in the Introduction, the ultimate goal must be to implement this knowledge of structures and energetics into a kinetic model for the whole nucleation and growth process.

ACKNOWLEDGMENTS

We thank Prof. G.D. Price, Dr. S.A. French, Dr. G. Sankar, Prof. Sir J.M. Thomas, Dr. A.R. George, and Dr. C.M. Freeman for helpful advice and discussions. We would also like to thank EPSRC and NERC for financial support and Accelrys for the provision of software.

REFERENCES

1. CRA Catlow, ed. Modelling of Structure and Reactivity in Zeolites London: Academic Press, 1992.
2. CRA Catlow, ed. Computer Modelling in Inorganic Crystallography San Diego: Academic Press, 1997.
3. RI Walton, F Millange, D O'Hare, AT Davies, G Sankar, CRA Catlow. J Phys Chem B 105: 83–90, 2001.
4. AL Yonkeu, V Buschmann, G Miehe, H Fuess, AM Goossens, JA Martens. Cryst Eng 4: 253–267, 2001.
5. P de Moor, TPM Beelen, RA van Santen. Micropor Mater 9:117–130, 1997.
6. WH Dokter, TPM Beelen, HF van Garderen, RA van Santen, W Bras, GE Derbyshire, GR Mant. J Appl Crystalber 27:901–906, 1994.
7. TPM Beelen, WH Dokter, HF van Garderen, RA van Santen, E Pantos. J Phys IV 3:393–396, 1993.
8. TPM Beelen, P Wijnen, CG Vonk, RA Vansanten. Catal Lett 3:209–215, 1989.
9. DMOL3, Accelrys, San Diego, 1996.
10. MJ Frisch, GW Trucks, HB Schlegel, PMW Gill, et al. Gaussian 94; Gaussian Inc., Pittsburgh, 1995.
11. Discover, Accelrys, San Diego, 1995.
12. InsightII, Accelrys, San Diego, 1996.
13. KD Keefer. In: Better Ceramics Through Chemistry (CJ Brinker, DE Clark, DR Ulrich, eds.). Materials Research Society. New York: Elsevier Science, 1984, p. 15.
14. G Orcel, L Hench. J Non-Cryst Solids 79:177–194, 1986.
15. CA Balfe, SL Martinez. In: Better Ceramics Through Chemistry II (CJ Brinker, DE Clark, DR Ulrich, eds.). Materials Research Society. New York: Elsevier Science, Vol. 73, 1986, p. 27.
16. JC Pouxviel, JP Boilot. J Non-Cryst Solids 94:374–386, 1987.
17. DR Tallant, BC Bunker, CJ Brinker, CA Balfe. In: Better Ceramics Through Chemistry II (CJ Brinker, DE Clark, DR Ulrich, eds.). Materials Research Society. New York: Elsevier Science, Vol. 73, 1986, p. 261.
18. SD Kinrade, TW Swaddle. Inorg Chem 27:4253–4259, 1988.
19. J Jonas. In: Ultrastructure Processing of Advanced Materials (DR Uhlmann, DR Ulrich, eds.). New York: Wiley, 1992, p. 13.
20. WG Klemperer, VV Mainz, DM Millar. In: Better Ceramics Through Chemistry II (CJ Brinker, DE Clark, DR Ulrich, eds.). Materials Research Society. New York: Elsevier Science, Vol. 73, 1986, p. 3.
21. WG Klemperer, VV Mainz, DM Millar. In: Better Ceramics Through Chemistry II (CJ Brinker, DE Clark, DR Ulrich, eds.). Materials Research Society. New York: Elsevier Science, Vol. 73, 1986, p. 15.

22. WG Klemperer, SD Ramamurthi. . In Better Ceramics Through Chemistry III. CJ Brinker, DE Clark, DR Ulrich, Eds.Materials Research Society, Elsevier Science Publishing Co.:, Vol. 121, 1988, pp 1.
23. WG Klemperer, VV Mainz, SD Ramamurthi, FS Rosenberg. In: Better Ceramics Through Chemistry III (CJ Brinker, DE Clark, DR Ulrich, eds.). Materials Research Society. New York: Elsevier Science, Vol. 121, 1988, p. 15.
24. CTG Knight. Zeolites 10:140–144, 1990.
25. LW Kelts, NJ Armstrong. J Mater Res 4:423–433, 1989.
26. JK West, BF Zhu, YC Cheng, LL Hench. J Non-Cryst Solids 121:51–55, 1990.
27. JK West, S Wallace, LL Hench, CR Lishawa. In: Ultrastructure Processing of Advanced Materials (DR Uhlmann, DR Ulrich, eds.). New York: Wiley, 1992, p. 111.
28. AC Lasaga, GV Gibbs. Phys Chem Miner 14:107–117, 1987.
29. AC Lasaga, GV Gibbs. Phys Chem Miner 16:29–41, 1988.
30. R Ahlrichs, M Bar, M Haser, C Kolmel, J Sauer. Chem Phys Lett 164:199–204, 1989.
31. J Sauer Chem Rev 89:199, 1989.
32. J-R Hill, J Sauer. J Phys Chem 98:1238–1244, 1994.
33. GV Gibbs, JW Downs, MB Boisen. Rev Mineral 29:331–368, 1994.
34. V Moravetski, JR Hill, U Eichler, AK Cheetham, J Sauer. J Am Chem Soc 118:13015–13020, 1996.
35. MS Stave, JB Nicholas. J Phys Chem 97:9630–9641, 1993.
36. I Papai, A Goursot, F Fajula, J Weber. J Phys Chem 98:4654–4659, 1994.
37. M Sierka, J Sauer. Faraday Disc 106:41–62, 1997.
38. JCG Pereira, CRA Catlow, GD Price. J Phys Chem A 103:3268–3284, 1999.
39. JCG Pereira, CRA Catlow, GD Price. J Phys Chem A 103:3252–3267, 1999.
40. BP Feuston, SH Garofalini. J Chem Phys 89:5818–5824, 1988.
41. BP Feuston, SH Garofalini. J Phys Chem 94:5351–5356, 1990.
42. SH Garofalini, G Martin. J Phys Chem 98:1311–1316, 1994.
43. U von Barth, L Hedin. J Phys C Solid State Phys 5:1629–1642, 1972.
44. L Hedin, BI Lundqvist. J Phys C Solid State Phys 4:2064–2083, 1971.
45. AD Becke. Phys Rev A 38:3098–3100, 1988.
46. CT Lee, WT Yang, RG Parr. Phys Rev B Condensed Matter 37:785–789, 1988.
47. B Delley. J Chem Phys 92:508–517, 1990.
48. AM Ferrari, P Ugliengo, E Garrone. J Phys Chem 97:2671–2676, 1993.
49. JD Kubicki, AC Lasaga. Am Mineral 73:941–955, 1988.
50. JD Dunitz, J Ibers Perspectives in Structural Chemistry II. New York: Wiley, 1968.
51. P Bornhauser, G Calzaferri. Spectrochim Acta A Mol Bio 46:1045–1056, 1990.
52. CRA Catlow, AR George, CM Freeman. Chem Commun 1311–1312, 1996.
53. W Lowenstein. Am Mineral 39:92, 1954.
54. PE Smith, BM Pettitt. J Phys Chem 98:9700–9711, 1994.
55. GM Zhidomirov, VB Kazansky. Adv Catal 34:131–202, 1986.
56. P Ugliengo, V Saunders, E Garrone. J Phys Chem 94:2260–2267, 1990.
57. BC Chakoumakos, GV Gibbs. J Phys Chem 90:996–998, 1986.
58. A Klamt, G Schüürmann. J Chem Soc Perkin Trans 2 799–805, 993.
59. J Andzelm, C Kölmel, A Klamt. J Chem Phys 103:9312–9320, 1995.
60. A Ben-Naim, Y Marcus. J Chem Phys 81:2016–2027, 1984.
61. J Sauer, M Sierka. J Comput Chem 21:1470–1493, 2000.
62. HA Stern, F Rittner, BJ Berne, RA Friesner. J Chem Phys 115:2237–2251, 2001.
63. RA Bryce, R Buesnel, IH Hillier, NA Burton. Chem Phys Lett 279:367–371, 1997.
64. P Sherwood, AH deVries, SJ Collins, SP Greatbanks, NA Burton, MA Vincent, IH Hillier. Faraday Disc 106:79–92, 1997.
65. M Krossner, J Sauer. J Phys Chem 100:6199–6211, 1996.
66. JCG Pereira, CRA Catlow, GD Price. Chem Commun 1387–1388, 1998.
67. AT Davies, G Sankar, CRA Catlow, SM Clark. J Phys Chem B 101:10115–10120, 1997.
68. AT Hagler, S Lifson, P Dauber. J Am Chem Soc 101:5122, 1979.
69. LB McCusker. Mater Sci Forum 133-136:423–434, 1993.

70. ML Connolly. J Appl Crystalbgr 16:548–558, 1983.
71. DW Lewis, CM Freeman, CRA Catlow. J Phys Chem 99:11194-11202, 1995.
72. RG Bell, DW Lewis, P Voigt, CM Freeman, JM Thomas, CRA Catlow. Computer Modelling of Sorbates and Templates in Microporous Materials. Zeolites and Related Microporous Materials: State of the Art 1994. Proceedings of the 10th International Zeolite Association Meeting, 1994, Amsterdam.
73. M Tsapatsis, M Lovallo, ME Davis. Micropor Mater 5:381–388, 1996.
74. S Mintova, NH Olson, V Valtchev, T Bein. Science 283:958–960, 1999.
75. R Boistelle, JP Astier. J Crystal Growth 90:14–30, 1988.
76. DH Gay, AL Rohl. J Chem Soc Faraday Trans 91:925–936, 1995.
77. O Terasaki. J Electron Microsc 43:337–346, 1994.
78. MW Anderson, JR Agger, JT Thornton, N Forsyth. Angew Chem Int Edit Engl 35:1210–1213, 1996.
79. JR Agger, N Pervaiz, AK Cheetham, MW Anderson. J Am Chem Soc 120:10754–10759, 1998.
80. B Slater, CRA Catlow, L Zheng, O Tetsu, O Terasaki, MA Camblor. Angew Chem Int Edit Engl 41:1235–1237, 2002.
81. Z Liu, T Ohsuna, O Terasaki, MA Camblor, MJ Diaz-Cabanas, K Hiraga. J Am Chem Soc 123:5370–5371, 2001.
82. MC Payne, MP Teter, DC Allan, TA Arias, JD Joannopoulos. Rev Mod Phys 64:1045–1097, 1992.
83. CRA Catlow, DS Coombes, DW Lewis, JCG Pereira. Chem Mater 10:3249–3265, 1998.
84. DW Lewis, CRA Catlow, JM Thomas. Faraday Disc 106:451–471, 1997.